INFLUENCE OF MATERIALS AND DESIGN PARAMETERS ON ZINC OXIDE SURFACE ACOUSTIC DEVICES

THESIS

Samuel DeWhitt, Captain, USAF

AFIT-ENG-MS-22-J-008

DEPARTMENT OF THE AIR FORCE
AIR UNIVERSITY

AIR FORCE INSTITUTE OF TECHNOLOGY

Wright-Patterson Air Force Base, Ohio

AFIT-ENG-MS-22-J-008

INFLUENCE OF MATERIALS AND DESIGN PARAMETERS ON ZINC OXIDE SURFACE ACOUSTIC DEVICES

THESIS

Presented to the Faculty

Department of Electrical and Computer Engineering

Graduate School of Engineering and Management

Air Force Institute of Technology

Air University

Air Education and Training Command

In Partial Fulfillment of the Requirements for the

Degree of Master of Science in Electrical Engineering

Samuel DeWhitt, B.S.E.E.

Captain, USAF

June 2022

DISTRIBUTION STATEMENT A.
APPROVED FOR PUBLIC RELEASE; DISTRIBUTION UNLIMITED.

AFIT-ENG-MS-22-J-008

INFLUENCE OF MATERIALS AND DESIGN PARAMETERS ON ZINC OXIDE SURFACE ACOUSTIC DEVICES

Samuel DeWhitt, B.S.E.E.

Captain, USAF

Committee Membership:

Dr. Hengky Chandrahalim, PhD
Chair

Dr. Kevin Leedy, PhD
Member

Dr. Guru Subramanyam, PhD
Member

AFIT-ENG-MS-22-J-008

Abstract

This thesis presents research into Zinc Oxide (ZnO) based resonators to include Width Extensional Mode (WEM), Length Extensional Mode (LEM), and Surface Acoustic Wave (SAW) devices. The design and operation of ZnO based SAW devices are investigated further to characterize design parameters and operating modes. Their design, fabrication, and results are discussed in detail. SAW device testing in conjunction with X-Ray Diffractometry (XRD) and Atomic Force Microscopy (AFM) are utilized to characterize ZnO and its deposition parameters on a variety of different substrates and interlayers, with different deposition temperatures and annealing parameters. These substrates include silicon, silicon oxide-on-silicon, and sapphire wafers with interlayers including titanium, tungsten, and silicon oxide. Fabrication methods are discussed to explain all processing steps associated with SAW and released contour mode resonators. The SAW devices in this research test different design parameters to establish better reflector design spacing for higher frequency Sezawa wave modes. The characterization and design of ZnO based SAW devices establishes the potential for prototyping high frequency SAW designs using standard lithography techniques. These devices are desired for space-based operations for use in GPS filters, signal processing, and sensing in satellites and space vehicles.

This work is dedicated to my family, friends and mentors who have supported me and guided me through my time at AFIT.

Table of Contents

List of Figures

List of Tables

List of Equations

INFLUENCE OF SILICON DIOXIDE ON SPUTTERED ZINC OXIDE GENERATED SURFACE ACOUSTIC WAVES

I. Introduction

1.1 Overview

As industry seeks to make devices smaller, lighter, and less power-hungry certain components on chips, and bulk components mounted on printed circuit boards need to be changed. Microelectromechanical Systems (MEMS) help to realize this change by helping replace bulky components like quartz crystal resonators with released resonators. MEMS are present in an ever-growing list of devices; some of the most commonly used MEMS devices exist in the telecommunications [1], medical [2][3], automotive [4], and printing industries [5]. These industries use MEMS for gas, fluid, pressure and temperature sensing [6][7], inertial measurement units (IMUs), motors, switches, and radio frequency (RF) filter and devices [8][9][10]. This thesis focuses on utilizing MEMS to make improvements to RF filtering devices for use in space applications like cube satellites. Two large focuses of cube satellites are weight and volume reduction. MEMS devices can be utilized to facilitate both requirements by replacing larger filters, oscillators, and amplifiers with monolithically integrated circuits containing significantly smaller components. MEMS devices can also be fabricated specifically to survive the high temperatures involved in space and the high temperatures and vibrations involved with space vehicle launches.

1.2 Motivation

Zinc Oxide (ZnO) is used to fabricate contour mode resonators (CMR) and surface acoustic wave resonators (SAWs). The research objectives and motivation behind this research are as follows:

- Characterize ZnO depositions to understand its potential as a high frequency, high-Q resonator material for space-based applications. Characterization Techniques include: Atomic Force Microscopy (AFM), Scanning Electron Microscopy (SEM), and X-Ray Diffraction (XRD).
- Validate ZnO depositions using simple, one mask, surface acoustic wave (SAW) devices to evaluate resonator characteristics prior to creating released devices.
- Design resonators targeting 1 to 2 GHz operating frequency using ‘in-house’ methods and equipment available. Characterize these devices using measured insertion losses (IL), quality factor (Q), and frequency tunability to measure their potential effectiveness as filter elements.
- Characterize released resonator devices based on their resistance to temperature, shock, and vibration to validate the potential for devices to be used in space-based payloads.

1.3 Research Contributions

This research validates past works in the field of SAW resonator device design and adds new contributions by charactering ZnO depositions by the use of several SAW device designs. These include:

- Developing a new method for placing SAW resonator reflector banks to enable lower insertion losses in high frequency modes. Depending on the device’s targeted frequency mode the reflector spacing can be set accordingly based on the ideal spacing found in this research.

- Creating a process flow to realize 800nm device features using standard lithography practices by direct writing onto a chip. These standard lithography techniques save the Air Force significant time and money since E-Beam lithography takes on the order of weeks for a new process rather than hours for standard lithography.
- Characterization of ZnO based SAW devices from 4 to 8 um λ to establish measured surface velocity for a given thicknesses of ZnO; this will be used for future research to build smaller devices at the ideal wavelength for the lowest insertion loss for a given device thickness.
- Determining the effectiveness of a given sample based on testing with XRD and AFM. Preliminary work using quick characterization techniques can help identify samples and depositions that will result in devices with poor performance or no useful characteristics at all. These depositions can be redone before more effort is put into fabricating multi-step released devices.

1.4 Thesis Overview

This thesis is broken up into 6 sections: Introduction, Literature Review, Fabrication Methodology, Testing Methodology, Results, and Conclusion. The second chapter will speak to past research and its impact on the decisions made for this research. Chapter three will discuss the methods used for each of the many fabrication steps in this research. Following that, chapter four will detail the testing set ups used to characterize the fabrication efforts. Results will be discussed in chapter five, and chapter six will offer final thoughts and recommendations for future students.

II. Literature Review

The literature review looks at past research conducted on MEMS devices, Zinc Oxide based resonators, deposition and fabrication techniques, simulations conducted to validate future devices development, as well as other research into specific fabrication steps along the way. This will look back to the 1980's when Zinc Oxide was first used as a SAW resonator material and look to the most recent developments into materials used for high frequency CMR and SAW devices.

2.1 MEMS as Resonators

MEMS resonators have been fabricated and tested since the mid-20th century and have transitioned from humble beginnings as resonating gate electrodes for transistors into the Nano world through NEMS fabrication. MEMS and NEMS resonator devices are now targeting frequencies in the 5-15 Ghz range [1][11][12]. MEMS resonators exploit the natural frequencies that each and everything vibrates at. Everything, depending on its shape, size, and material resonates at some frequency; MEMS utilize this idea and apply it at a small scale. Just as a simple cantilever, like a tree branch, will oscillate after an impulse is applied to it, so too will a micro-cantilever. The composition of these cantilevers and their size dictates their resonant frequency. However, everything resonates regardless of its shape and size; MEMS resonators take many shapes and sizes from cantilevers to parallel plates, bars, and material surfaces themselves.

2.2 MEMS Resonator Theory of Operation

Radio Frequency MEMS resonators work based on three main theories of operation: Capacitive or Electrostatic Transduction, Piezoelectric Transduction, and

Ferroelectric Transduction. Only Electrostatic and Piezoelectric transduction methods will be discussed.

2.2.1 Electrostatic (Capacitive) Transduction

Electrostatically transduced RF MEMS resonators operate based on an induced strain in the device by way of a DC electric field applied between the resonator and a drive electrode. This DC field has an RF signal superimposed which generates small changes in the DC electric field; when the RF signal is matched to the device’s resonant frequency it will oscillate at a particular mode. Most devices have more than one resonant frequency and associated mode. These devices can be fabricated out of low acoustic loss materials such as polysilicon and single crystal silicon to achieve high quality factors [13]. However, these devices require extremely tight fabrication tolerances to achieve these high Q values; this is due to the motional resistance of the device growing by the fourth power as the gap between the drive electrode and resonator body increases [14]. These devices can be fabricated using movable drive and sense electrodes and larger fabrication tolerances but those can have their own fabrication and actuation issues [15]. Finally, electrostatically driven devices can have a high-k dielectric material deposited in between the drive electrode and the resonator body to improve the transduction; this can lead to some improvements over devices with an airgap between the electrodes, but the dielectric material can act as another damping source that increases the motional resistance as well as decreasing the Q-factor of the device. Some dielectric layers help to improve the Q-factor of the device at sufficiently small enough operating frequencies. Each situation is dependent on the material selection and device shape [16]. In general, as the frequency of operation increases, the size of the resonator device decreases, decreasing the area of transduction between the electrode and the resonator body, and increasing the motional resistance. At higher frequencies these devices become less feasible than their piezoelectric or ferroelectric counterparts.

2.2.2 Piezoelectric Transduction

Piezoelectric MEMS resonators operate using the piezoelectric effect and the inverse piezoelectric effect in which an electric field applied generates a strain in the material and a strain in the material generates an electric field. That electric field, when applied at a resonant frequency, generates repeated strain which in turn generates waves in the material that propagate through the bulk or the surface and generate electric fields; these waves can be generated by one electrode and their resulting electric fields sensed by another. The main benefit of piezoelectric transduction is the simpler fabrication process and potential for higher operating frequencies as their motional resistance is dictated by the piezoelectric coupling constants rather than the transduction gap between electrodes on electrostatic devices. Unlike electrostatically driven resonators, piezoelectric resonators tend to have the electrode material directly attached to the piezoelectric material.

Piezoelectric materials couple the electrical and mechanical behaviors of a material together. The electrical behavior of a material is dictated by:

$$D = \varepsilon E$$

Equation 1

Where D is the electrical displacement, ε is the permittivity of the material, and E is the electrical field strength [14]. The mechanical behavior of a material is in turn dictated by:

$$S = sT$$

Equation 2

Where S is the strain, s is the compliance of the material, and T is the stress on the material. Piezoelectric materials combine and couple these equations together by the piezoelectric constant d, the permittivity at a constant stress ε^T, and the compliance at a constant electric field s^E. This results in the following equations:

$$D = \varepsilon^T E + dT$$

Equation 3

$$S = d^t E + s^E T$$

Equation 4

As a note, in the equations above, d^t is the transpose of the piezoelectric constant matrix and not a separate variable. These equations can be broken out into their Strain-Charge matrix as shown in the figure below:

$$\begin{pmatrix} S_{xx} \\ S_{yy} \\ S_{zz} \\ S_{yz} \\ S_{xz} \\ S_{xy} \end{pmatrix} = \begin{pmatrix} s_{E11} & s_{E12} & s_{E13} & s_{E14} & s_{E15} & s_{E16} \\ s_{E21} & s_{E22} & s_{E23} & s_{E24} & s_{E25} & s_{E26} \\ s_{E31} & s_{E32} & s_{E33} & s_{E34} & s_{E35} & s_{E36} \\ s_{E41} & s_{E42} & s_{E43} & s_{E44} & s_{E45} & s_{E46} \\ s_{E51} & s_{E52} & s_{E53} & s_{E54} & s_{E55} & s_{E56} \\ s_{E61} & s_{E62} & s_{E63} & s_{E64} & s_{E65} & s_{E66} \end{pmatrix} \begin{pmatrix} T_{xx} \\ T_{yy} \\ T_{zz} \\ T_{yz} \\ T_{xz} \\ T_{xy} \end{pmatrix} + \begin{pmatrix} d_{11} & d_{21} & d_{31} \\ d_{12} & d_{22} & d_{32} \\ d_{13} & d_{23} & d_{33} \\ d_{14} & d_{24} & d_{34} \\ d_{15} & d_{25} & d_{35} \\ d_{16} & d_{26} & d_{36} \end{pmatrix} \begin{pmatrix} E_x \\ E_y \\ E_z \end{pmatrix}$$

$$\begin{pmatrix} D_x \\ D_y \\ D_z \end{pmatrix} = \begin{pmatrix} d_{11} & d_{12} & d_{13} & d_{14} & d_{15} & d_{16} \\ d_{21} & d_{22} & d_{23} & d_{24} & d_{25} & d_{26} \\ d_{31} & d_{32} & d_{33} & d_{34} & d_{35} & d_{36} \end{pmatrix} \begin{pmatrix} T_{xx} \\ T_{yy} \\ T_{zz} \\ T_{yz} \\ T_{xz} \\ T_{xy} \end{pmatrix} + \epsilon_0 \begin{pmatrix} \epsilon_{rT11} & \epsilon_{rT12} & \epsilon_{rT13} \\ \epsilon_{rT21} & \epsilon_{rT22} & \epsilon_{rT23} \\ \epsilon_{rT31} & \epsilon_{rT32} & \epsilon_{rT33} \end{pmatrix} \begin{pmatrix} E_x \\ E_y \\ E_z \end{pmatrix}$$

Figure 1: Strain Charge Matrix for a generic piezoelectric device.

The matrix above has several constants that will be zero or will be the negative of the constant with a reversed subscript, i.e, $d_{31} = -d_{13}$. The subscripts associated with each of the piezoelectric constants, permittivity constants, and the compliance constants represent the x, y, and z axis as well as the rotation about each axis. This can be visualized in the figure below:

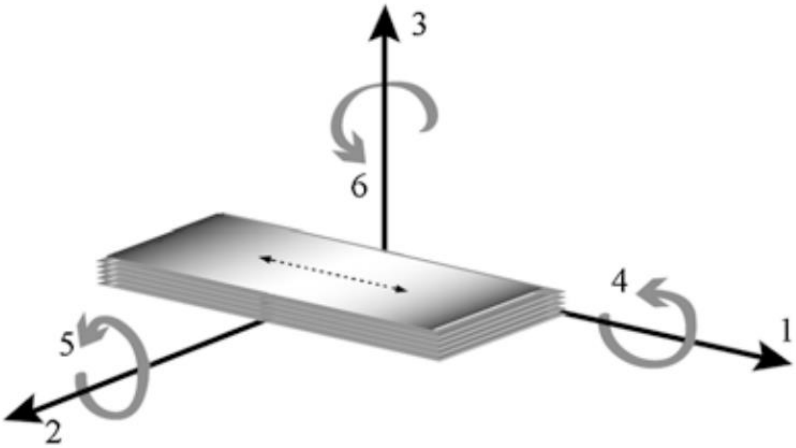

Figure 2: The six subscripts of the Strain-Charge Matrix and their representations on a generic object.

All piezoelectric constants will influence a device’s overall operation, but in certain operating modes a given d_{ij} can be used to calculate the effect while the rest ignored. This is discussed more below.

2.3 MEMS Resonator Operating Modes

2.3.1 Operating Modes for Released Resonator Devices

There are several different resonator operating modes that could be discussed. These include but are not limited to: width, length, and thickness extensional modes [17], shear horizontal modes [18], lamb wave modes [1], distributed Lame Modes [19], etc. In the released devices section of this research the focus is on Width Extensional (WEM), Length Extensional (LEM), and Thickness Extensional (TEM) modes. WEM, LEM and TEM modes are excited by electrodes place above and below the piezoelectric material and their frequencies of operation are determined by the thickness of the thin film, the width and length of the device, as well as the thickness and material of the electrodes. Width extensional mode and length extensional modes are determined by the s_{E31} and d_{31}, the compliance and piezoelectric constants. The subscript, 31, represents the effect of strain or electric field applied across the z-axis and the resulting electric field or strain in the x-axis. When designing devices for thickness extensional modes the subscript 33 constants are utilized which represent the field or strain applied in the z-axis and resulting strain or field in the z-axis. It is important to note that all three modes may be present on a single device, and coupling effects exist between the modes; some new modes may be excited by this coupling effect.

One downside of the Thickness Extensional Modes is that the frequency of operation is set by the thickness of the piezoelectric material (ferroelectrics will have slight tuning potential) rather than the width or the length of the designed device. This means that for a given deposition of thin film, the thickness mode frequency is fixed and determined by Equation 12 with W being replaced with T, representing the thickness of that thin film. However, TEM modes have been shown to operate at higher frequencies in past works [20][21] and those high frequencies are reached with high Q-factors without relying on higher overtones like width and extensional modes. Width and Length Extensional modes and their design are discussed more in section 3.6.

2.3.2 Operating Modes for Surface Acoustic Wave Devices

Like released devices, there are several operating modes in SAW devices. The most prevalent SAW design rules focus on exciting the Rayleigh and Sezawa operational modes. These modes have been studied since the 1980's and have thousands of documents published on the matter [8], [9], [10], [17], [18]. Additionally, love wave modes and other shear-horizontal based modes allow for more transduction methods and operational frequencies [8]. SAW devices utilize interdigitated transducers (IDTs) to generate localized strain in the surface of a thin piezoelectric, or properly biased ferroelectric material. The repeated strain generated by the electric field between the signal and ground IDTs causes surface waves to form and propagate laterally from the orientation of the IDTs. These waves can move 'up and down' relative to the surface of the material (Rayleigh and Sezawa) or side to side as the wave progresses (Shear-Horizontal / Love)

2.4 Quality Factor of MEMS Resonators

The quality factor of a MEMS resonator depends on several different quality factors combined. The overall quality is dependent on the quality of the thin film, the surface losses, anchor losses, and environmental losses due to air. The quality factor (Q) can be represented by the following equation:

$$\frac{1}{Q} = \frac{1}{Q_{AKE}} + \frac{1}{Q_{TED}} + \frac{1}{Q_{ANC}} + \frac{1}{Q_{SURF}} + \frac{1}{Q_{AIR}}$$

Equation 5

Each of the Q parameters on the right side of the equation influences the overall Q-Factor of the device. Each of these is minimized in designs or testing to achieve the highest Q possible. Q_{AKE} represents the Akhiezer damping present in all materials. This damping is due to phonon scattering in the material and the absorption of acoustic waves.

Q_{TED} represents the loss of energy due to thermoelastic damping (TED) and is dependent on the temperature that the device is operated at. TED is material dependent and is effectively the change of acoustic wave energy into heat based on the device's thermal expansion coefficient at a given temperature of operation. If the device is operated at a temperature in which the resonant material has a large thermal expansion coefficient, the quality factor of the resonant peak will decrease as more energy is lost to heat [24].

Q_{ANC} is the loss associated with anchors used to suspend released resonator devices. The Q_{ANC} losses are characterized by the size of the anchors as well as the wavelength of operation in the device at resonance. The energy transmitted from the device into the anchors and bulk substrate characterizes the anchor loss. By designing these anchors to be smaller than the device and at one quarter of the wavelength of operation the amount of energy lost through the anchors is minimized.

Q_{SURF} is the loss due to the surface of the device. Roughness in the surface, as well as microporosity and cracking induce damping at the surface layer. It was found that for two devices at the same operating frequency, the device with a larger surface area had a lower Q due to the larger surface losses experienced [25]. By reducing the surface area of the device and improving deposition parameters to yield lower surface roughness, Q_{SURF} can be minimized.

Q_{AIR} is the loss of quality factor due to the air resistance and damping on the movement of the device under resonance. This can be reduced by operating the devices under vacuum to reduce the Q_{AIR} component of overall quality factor.

2.5 Material Selection

2.5.1 Piezoelectric Layer

Zinc Oxide (ZnO) was selected for this research due to its ability to be fabricated into a wide variety of different devices. Its versatility allows multiple types of devices to all be fabricated on one chip together and directly integrated with other technologies. Specifically, ZnO can be used to make thin-film-transistors [26][27] and resonator devices and filters; this enables the integration of device power handling, signal filtering, signal processing, and logic together on one monolithically integrated circuit.

In addition to its integration potential, ZnO can be deposited by several methods to realize large d_{31} and d_{33} piezoelectric coefficients. These methods include sputtering ZnO directly [28][29], sputtering Zinc and growing a thermal oxide [30], chemical vapor deposition [31], atomic layer deposition [27], and pulsed laser deposition [32][33][34].

Finally, ZnO was chosen due to its high melting temperature of 1975°C making it an exceptional candidate for high-temperature space environments.

2.5.2 Wafers

100-Silicon wafers, SiO_2-on-Silicon wafers, and Sapphire (Al_2O_3) wafers were all utilized in this research. Wafer selection impacts devices differently. For released devices, the wafer is selected with a sacrificial layer in mind. Silicon and Silicon Oxide are both materials that can be used as a sacrificial layer in the release of resonator devices as they can both be laterally etched by Xenon Difluoride and Hydrofluoric Acid respectively. Sapphire wafers were not utilized for released devices due to the specialized equipment required to isotopically etch sapphire.

For surface acoustic wave devices, the wave velocity and stiffness of the substrate dictates the effective wave velocity of the thin film used. 100-Silicon, SiO_2-on-Silicon, and Sapphire wafers were all tested to measure the impact of substrate selection on the surface acoustic wave velocity of the fabricated devices.

Substrates were also tested based on their ability to align deposited ZnO with its preferred (002) basal plane orientation [35]. The c-axis growth of ZnO, normal to the (002) plane is indicative of excellent piezoelectric properties. The c-axis growth of ZnO on three different wafers and several interlayers is discussed later in this research. In addition to having excellent etching properties, SiO_2 layers have been shown to improve ZnO growth on top of metal layers

2.5.3 Metal Layers

The bottom and top metal electrodes have a large impact on the application of the desired device. Operating temperature, deposition parameters, sheet resistance all factor into the feasibility of the metal being used for fabrication. With a desire for higher temperature thin films for use in space-based applications, tungsten was an obvious choice due to its high melting point. As seen below in a chart of metals and some of their key parameters, tungsten has an acoustic velocity of 5180 m/s making it a close acoustic match for ZnO. Aluminum and Zinc metals would not be feasible for space applications due to their relatively low melting temperatures, but their acoustic velocities would make them viable for lower temperature applications with ZnO.

Material	**Acoustic Velocity (m/s)**	**Melting Temperature °C**
Aluminum	6320	660.3
Gold	3240	1064
Molybdenum	6250	2623
Nickel	5630	1455
Platinum	3260	1768
Titanium	6100	1668
Tungsten	5180	3422
Zinc	4170	419.5

Table 1: Various metals available for use based on established evaporation and sputtering techniques. The acoustic velocities and melting temperatures are compared above.

2.5.4 Interlayers

To facilitate the c-axis deposition of ZnO on Tungsten, two interlayers are investigated. Titanium (Ti) and Silicon Oxide (SiO_2) are investigated further in this research for use in contour mode released resonator devices. Previous work has established that in addition to having excellent etching properties, SiO_2 layers have been shown to improve ZnO deposition on top of metal layers. While SiO_2 has been shown to make an excellent base for ZnO growth directly or improved ZnO deposition on top of metals [29], it has not been established if an SiO_2 interlayer between bottom tungsten metal and ZnO would benefit ZnO growth. Platinum layers saw an improvement with a thin oxide layer deposited on top [14]; an oxide layer on top of tungsten will be investigated in this research. Additionally, Ti evaporated on top of gold has helped improve the c-axis growth of ZnO and it will also be investigated as a potential interlayer between the ZnO and the tungsten metal.

III. Methodology

3.1 Chapter Overview

This chapter provides the design and fabrication processes that were utilized to fabricate both Surface Acoustic Wave (SAW) and released Contour Mode Resonator (CMR) devices.

3.2 SAW Resonator Design

Two port SAW devices were designed and fabricated for testing in this research; these devices can be fabricated with several ports but are typically designed in the one or two port variety. The two port resonators in this research operate by creating a stress field on the surface of the thin film via one set of interdigitated transducers (IDTs) and a Radio Frequency (RF) signal; the stress field creates surface waves that emanate laterally in both directions. The second set of IDTs are stressed by the incoming waves and, if properly designed, generate an electrical response sensed on the second port. To best capture the surface wave energy a set of reflectors is placed on either side of the two-port resonator which help reflect surface waves back towards the first and second ports. The insertion loss of a device can be reduced when more wave energy is reflected into the device rather than lost through the bulk of the substrate. Therefore, it is critical to design and fabricate SAW devices using the following set of design rules which minimize the amount of energy lost to the bulk of the substrate or lost to destructive interference of the waves with one another.

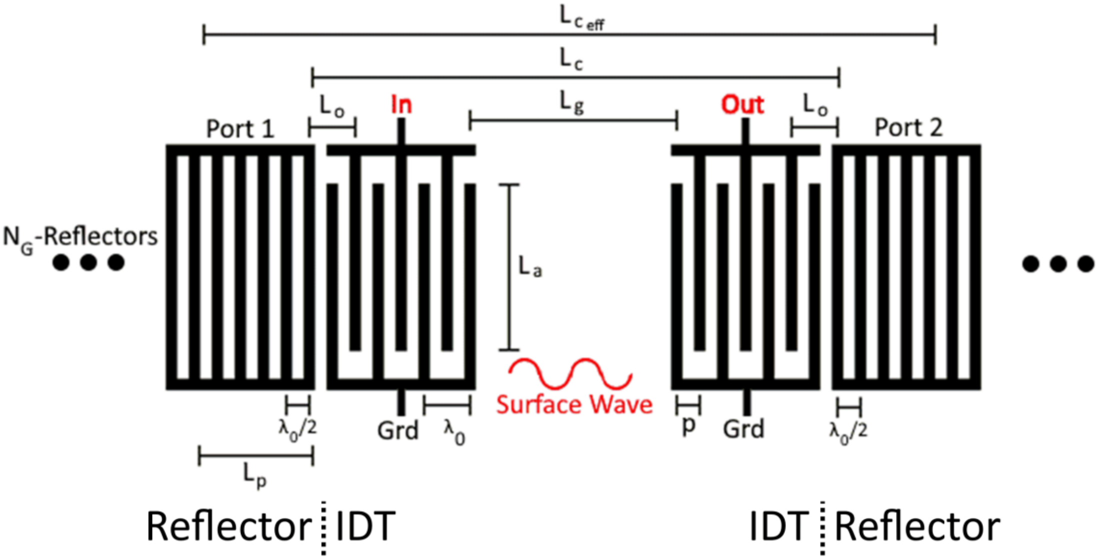

Figure 3: Critical dimensions for Surface Acoustic Wave resonator design. Each labeled dimension is calculated below based on the targeted first frequency of operation f_0 and other material specific parameters. This image is formatted to show each parameter clearly and as such is not scaled to represent final devices.

The first resonant frequency of operation, also known as the Rayleigh 0th order mode is calculated based on the spacing of the IDTs and the acoustic velocity of the substrate. This first resonant frequency, f_0, is given by:

$$f_0 = \frac{v_m}{\lambda_0}$$

Equation 6

Where v_m is the acoustic velocity of the substrate and λ_0 is wavelength. The remaining design parameters were based on the work of Datta [36] and on the work of Morgan [37].

The spacing between the two ports of the resonator, L_g, should be set such that it is equal to an integer multiple of one-half wavelength. When it is set at values equal to an integer multiple of one wavelength the device will operate 180 degrees out of phase from devices made to integer multiples of one-half wavelength. The length of the cavity between the two ports is designed such that the waves constructively interfere at the electrodes. At any cavity lengths other than multiples of one-half wavelength the stress induced by the surface waves occurs between IDTs and is not translated into back into the electrical domain at the location it can be sensed.

The spacing between the ports of the resonator and their respective reflector is calculated similarly to the cavity spacing, such that the surface waves reflecting off them constructively interfere with the IDTs. This is set such that:

$$L_0 = N\frac{\lambda_0}{2} + \frac{3\lambda_0}{8}$$

Equation 7

Where N is an integer value. This spacing ensures that the most energy possible is reflected back towards the device and is not dissipated into the bulk of the thin film. The overall spacing of the SAW cavity length, L_{Ceff} is the sum of L_c and $2L_p$. This spacing should be set such that the SAW device forms a Fabry-Perot cavity in which the waves approach unity reflectivity within the cavity; this assures that the surface wave energy transmits from one port to the other with minimal leakage into the bulk of the thin film. Additionally, L_{Ceff} should be set such that it is an integer multiple of one-half wavelength. Therefore, the resonant cavity should be set such that both of the following equations are satisfied:

$$L_{ceff} = 2L_p + L_c$$

Equation 8

$$L_{ceff} = N\frac{\lambda_0}{2}$$

Equation 9

To calculate the size of the reflectors L_p some assumptions on device and material properties need to be made. The precise calculation of L_p is given by the equation:

$$L_p = \frac{\tanh\left((N_G - 1) * r_s\right)\lambda_0}{4 * r_s}$$

Equation 10

Where N_G is the number of reflector gratings and r_s is the acoustic reflectivity of a single reflector grating. This should be set based on the wavelength of the device and the reflectivity of the metals used for the reflectors. The equation for finding the acoustic reflectivity is below:

$$r_s = a + b * \frac{h}{\lambda_0}$$

The variables a and b are material specific parameters that change based on the metals selected or annealing parameters. The variable h is the height of the reflector metal. In this case these parameters are unknown and the materials in this work were not characterized to find the best number of reflector gratings beforehand. If it is assumed that the number of reflector gratings, $N_G \rightarrow \infty$, equation 5 is simplified to:

$$L_p = \frac{\lambda_0}{4 * r_s}$$

Equation 11

Without knowing the best reflector grating count, an assumption was made that the reflectivity of each grating, r_s was somewhere between 0.005 and 0.010. For devices operating with wavelength $\lambda_0 = 8\ um$ an estimated penetration depth between 200um and 400um is assumed; this would require $50 < N_G < 100$. To maximize the likelihood of forming a Fabry-Perot cavity each reflector array was sized such that $N_G = 100$.

The cavity length of the resonator is tied to the quality (Q) factor of the device with Q increasing with an increased cavity length. To maximize the number of devices built on a single sample the cavity length was set to the minimum possible size by Equation 8 and Equation 9 above; larger cavity sizes were not tested.

3.3 Zinc Oxide Thickness Considerations

The thickness of the ZnO thin film plays a key role in establishing the electromechanical coupling coefficient of the material for surface acoustic wave devices. The electromechanical coupling coefficient (k^2) is a proportional measure of the conversion efficiency between electrical and mechanical energy in a piezoelectric material, or the energy converted per input energy. Each device has its own k^2 based on the resonator type, design, as well as the ZnO deposition quality and thickness. Additionally, the substrate that the ZnO is deposited on can drastically change the k^2 value as well; certain substrates and thin films absorb more energy than others. The more energy that is dissipated through the thin films, the lower the k^2 will be.

The ZnO thickness of the device also changes the surface wave velocity of the device. For a given device wavelength, as the thickness of the substrate is changed the frequency of operation for that device will change too.

3.4 COMSOL Finite Element Analysis for SAW Devices

COMSOL Multiphysics was utilized in this research to simulate and identify the different modes shapes of operation, as well as their operating resonant frequencies.

Different substrates, ZnO thicknesses, and electrode materials and thicknesses were tested in COMSOL. Some of the devices modeled in this research are shown below. COMSOL modeling will be discussed more in the results section of the research and mode shapes associated with various frequency peaks will be displayed.

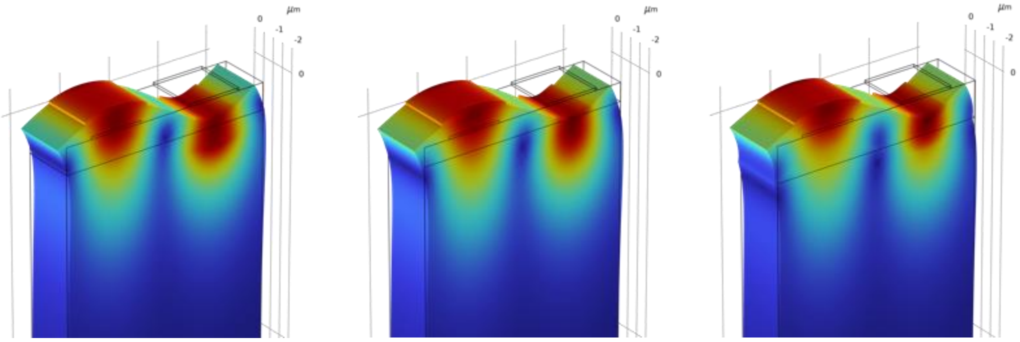

Figure 4: Silicon Oxide-on-Silicon, Silicon, and Sapphire Substrates with Zinc Oxide and Gold electrodes on top. The Rayleigh resonant mode is shown for each of the substrates with 8 micron λ devices. The fundamental Rayleigh frequency of each of the devices is 334.5 MHz, 483.8 MHz, and 558.0 MHz, respectively.

3.5 Released Contour Mode Resonator Design

Released Contour Mode Resonator (CMR) devices are constructed with a bottom metal electrode, a piezoelectric or ferroelectric material, and top electrodes. The electrodes and the material are patterned into a shape that will either operate in a Length Extensional Mode (LEM) or Width Extensional Mode (WEM). Additionally, these devices will most likely have an inherent Thickness Extensional Mode (TEM) that may or may not be excited due to the layout of the top and bottom metal electrodes. There are a multitude of other released device architectures, but this research focused on two of the more basic architectures. LEM and WEM devices are effectively the same type of architecture rotated 90 degrees; they are both extensional modes that, in their first order, extend laterally away from the center of the device. The edges spread apart, and the center of the device gets thinner. Higher order LEM and WEM modes can also be excited and behave much like the first order with more wave periods. The frequency of operation of these modes can be calculated based on the following equation:

$$f_0 = \frac{1}{2W}\sqrt{\frac{k_{eff}}{m_{eff}}}$$

Equation 12

Where f_0 is the fundamental frequency of operation, k_{eff} is the effective stiffness of the device, and m_{eff} is the effective mass of the device. W is the width of the device; in this case width, length, or thickness could be substituted into this equation to calculate for each of the fundamental modes of operation. Thickness Extensional Modes (TEM) were not utilized since the thickness of the device is set by the thickness of the piezoelectric thin film and can’t be modified after deposition. Width and length parameters can be changed to target specific frequencies; it’s noted that to target higher frequencies, the width or length needs to be decreased or a higher order mode needs to be excited. This research used designs to target 23 MHz, 52.5 MHz, and 115 MHz WEM and LEM devices which correlated to round numbers for W, L, and T. These device frequencies were chosen due to their simpler fabrication and lithography compared to smaller devices with higher frequencies of operation. These would be used to characterize the thin film and then higher frequency devices would be built targeting 1-2 GHz.

There are many ways to achieve a target frequency. For a WEM device the width is set to establish the fundamental frequency. For a given device the thickness and length will dictate their own operating frequencies, but their actual dimensions do not change the WEM frequency as seen in equation 2 above. Likewise, in a LEM device the width and thickness do not change the LEM frequency of operation. However, each parameter can have a significant change to the motional resistance, inductance, capacitance, and parasitic capacitance as seen in the equations below:

$$R_m = \frac{\sqrt{k_{eff} * m_{eff}}}{Q\eta^2}$$

Equation 13

$$L_m = \frac{m_{eff}}{\eta^2}$$

Equation 14

$$C_m = \frac{\eta^2}{k_{eff}}$$

Equation 15

$$C_0 = \frac{W * L * k * \varepsilon_0}{T}$$

Equation 16

Where R_m, L_m, and C_m are the motional resistance, inductance, and capacitance, and C_0 is the parasitic feed-through capacitance. W, L, and T are the width, length, and thickness of the device, k is the dielectric constant of the piezoelectric, and ε_0 is the permittivity of free space. The following equations for η^2, m_{eff}, and k_{eff}, need to be solved to calculate the motional parameters. The equations are all based on material properties, as well as the width, length, and thickness of the designed device:

$$\eta^2 = (2 * d_{31} * W * E)^2$$

Equation 17

$$m_{eff} = \frac{\rho * \mathrm{W} * \mathrm{L} * \mathrm{T}}{2}$$

Equation 18

$$k_{eff} = \frac{\pi^2 * E * L * T}{8 * W}$$

Equation 19

Where η^2 is the piezoelectric coupling constant, m_{eff} is the effective mass of the designed resonator, k_{eff} is the effective stiffness of the resonator, and d_{31} is the piezoelectric coefficient for strain in the x-direction from an electric field applied in the z-direction; in this case electrodes on the top and bottom are used to apply the field. E is the Young’s Modulus of Zinc Oxide, and ρ is the density.

When designing a WEM resonator the desired operating frequency determines the width, and the material properties are set intrinsically. Therefore, it is critical to design the remaining parameters to minimize the motional resistance and maximize the capacitance. Each of these parameters is linked together by the equations above so the design process is a balance between operating frequency and motional parameters. If the motional resistance is too high the device may operate below the noise floor of the test equipment. Additionally, if the motional capacitance is too low the feed-through capacitance will dominate and result in a resonator that is useless for practical filtering applications as the device will act as a bandpass for any frequencies just higher than the resonant frequency. These two effects can be seen below:

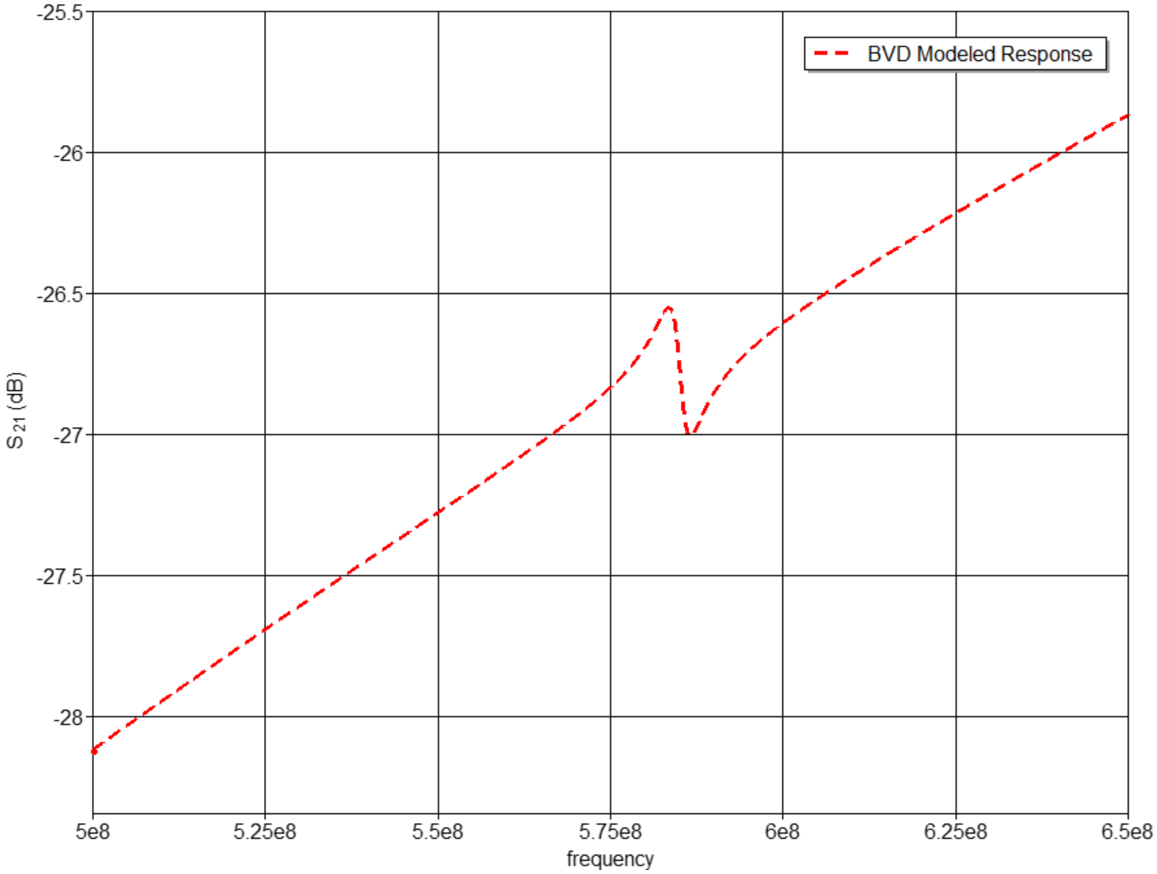

Figure 5: Example of a poorly quality resonator modeled in QUCS Studio. A high motional resistance causes peak to be small and the insertion loss to be large while the larger parasitic capacitance causes the device's noise floor to rise with frequency effectively making the resonator useless.

3.6 COMSOL Finite Element Analysis for Released Contour Mode Devices

COMSOL was used to analyze released contour mode devices. The parameters used were the same as those used in the simulation of SAW devices. At higher frequencies, many different modes can exist close to the desired frequency of operation. At lower frequencies, resonant modes can be viewed cleanly as shown in the figure below:

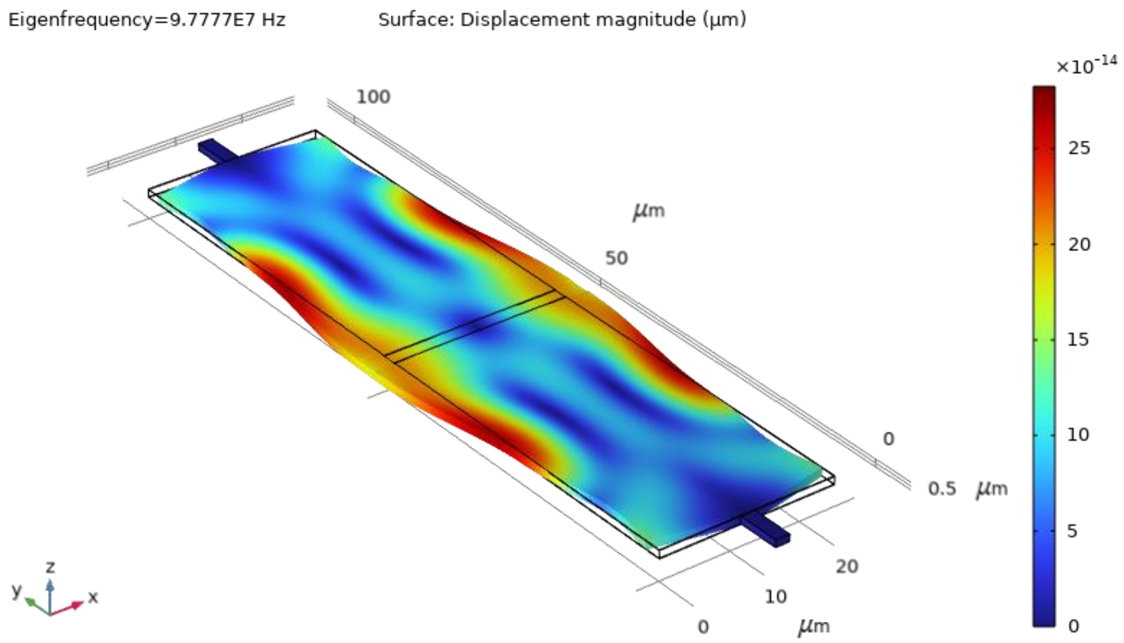

Figure 6: COMSOL FEA of WEM Released Resonator with fixed tethers. Rollers are applied to the top and bottom faces of the device in order to visualize only the WEM and LEM modes. Displayed above is the fundamental WEM mode at a designed frequency of 100 MHz.

At higher frequencies these modes get exceptionally difficult to visualize, even with several constraints applied to the model; these constraints typically are fixed planes such that the device will not move in a particular direction. Below are two higher frequency simulations that show the difference between constrained and unconstrained thickness planes:

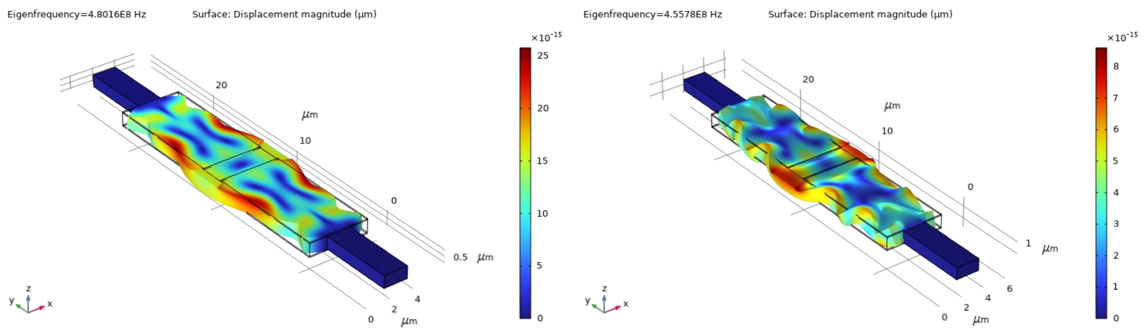

Figure 7: Comparison of two COMSOL FEAs of WEM resonators with a designed frequency of 500 MHz. The WEM on the left is simulated using roller constraints on the top and bottom of the released resonator while the image on the right has those constraints removed. The constrained resonator had a WEM frequency of 480.1 MHz while the unconstrained simulation had a WEM frequency of 455.7 MHz.

The unconstrained model has several frequency modes overlapping that make it more difficult to identify a particular mode. Additional COMSOL simulations will be addressed in the results portion of this paper.

3.7 Fabrication Processes for Zinc Oxide Resonators

Fabrication of ZnO resonators is divided into the various steps required to fully realize released devices. Surface Acoustic Wave (SAW) devices use the same fabrication steps as released devices but omit any etching of the thin film or substrate below it. SAW devices are built entirely on the surface of the piezoelectric layer and require no etching of the substrate or bottom metal layers. This fabrication methodology is organized in sequential order; the first processing steps required will be listed first and the last processing steps will be listed last. Some processes described in this section happen concurrently; these are listed alphabetically.

The fabrication flows for released resonators and SAW resonators are listed below. Each of the fabrication steps are further broken down into more detail and the parameters associated with each step and its associated processes is discussed.

Released Resonator Process Flow:

1) Deposit bottom metal onto chosen wafer via sputtering or evaporation
2) Deposit interlayer on top of bottom metal via sputtering, evaporation, or chemical vapor deposition
3) Deposit Zinc Oxide via sputtering
4) Dice wafer into 15mm x 15mm squares
5) Spin photoresist onto chips
6) Perform direct write or mask alignment step to pattern features – MASK 1
7) Develop chip
8) Plasma ash chip
9) Etch Zinc Oxide to establish ground vias
10) Clean Photoresist off and spin next layer on
11) Perform direct write or mask alignment step to pattern features – MASK 2
12) Develop chip
13) Plasma ash chip
14) Deposit top metal via sputtering or evaporation
15) Perform Metal Liftoff
16) Clean Photoresist and spin next layer on
17) Perform direct write or mask alignment step to pattern features – MASK 3
18) Develop chip
19) Plasma ash chip
20) Etch Zinc Oxide to establish resonator size and shape
21) Etch interlayer
22) Etch bottom metal
23) Perform release step by etching away wafer below bottom metal
24) Clean photoresist
25) Perform Critical Point Dry
26) Test Devices

Surface Acoustic Wave Resonator Process Flow:

1) Deposit Zinc Oxide via sputtering
2) Dice wafer into 15mm x 15mm squares
3) Spin photoresist onto chips
4) Perform direct write or mask alignment step to pattern features – MASK 1
5) Develop chip
6) Plasma ash chip
7) Deposit top metal via evaporation

8) Perform Metal Liftoff
9) Clean Photoresist
10) Test Devices

As it can be seen in the processing steps above, released resonators require at least 3 masks or direct write steps to fully fabricate the devices while SAW devices require just one mask or direct write to fully fabricate.

3.7.1 Tungsten Sputtering

For released devices, the first step is to deposit the bottom electrode metal onto the wafer. Tungsten was chosen for its extremely high melting point and similar acoustic velocity as discussed earlier.

The properties of a sputtered film drastically change depending on the deposition rate, temperature of the substrate, power supply wattage, and chamber pressure. Targeting specific properties is difficult and most processes need to be characterized and tested extensively to fully realize a particular property. The parameters used for sputtering Tungsten at are below:

Parameter	**Value**
Ignition Capman Pressure (mTorr)	10
Ar Gas Flow (sccm)	4
Power Supply (watts)	100
Running Capman Pressure	8
Burn in time (seconds)	60
Substrate Rotation (rpm)	5
Deposition Time (seconds)	1200
Deposition Rate (nm/minute)	5.7
Nominal Thickness (nm)	114

Table 2: Tungsten metal deposition parameters using at Kurt J. Lesker Sputtering System

3.7.2 Silicon Oxide Chemical Vapor Deposition

Some substrates used in this research were coated with Tungsten metal as a bottom layer. ZnO growth on Tungsten was tested in preliminary research and did not result in working devices; therefore an interlayer of SiO_2 was deposited since its addition showed an improvement in the XRD peak intensity of the ZnO thin film [38]; Two substrates were tested with this process. 50 nanometers (nm) of SiO_2 was deposited on top of tungsten metal using Plasma Enhanced Chemical Vapor Deposition (PE-CVD). This deposition process uses SiHe in conjunction with oxygen, O_2 to deposit SiO_2 onto the surface of the substrate. In addition to the gas flow rates, chamber pressure, and the plasma power, the chamber can also be heated to change deposition rates and film qualities. This SiO_2 layer was only utilized on released resonator devices with bottom metal. The PE-CVD process parameters are listed below:

Parameter	**Value**
Chamber Pressure (mTorr)	900
SiHe Gas Flow (sccm)	160
N_2O Gas Flow (sccm)	900
Plasma Power (watts)	25
Deposition Rate (Å/minute)	475
Deposition Time (seconds)	63
Nominal Thickness (nm)	50

Table 3: Plasma Enhanced Chemical Vapor Deposition Parameters for SiO_2 thin film deposited in a Plasma-Therm 790 Series PE-CVD.

3.7.1 Titanium, Gold, and Aluminum Evaporation

Metal Evaporation is used to deposit thin films of metal with high directionality and low sidewall passivation. Titanium metal was used as another method to improve ZnO c-axis growth. Like SiO_2, a titanium layer of metal between the tungsten and the ZnO showed better plane geometry than ZnO on tungsten alone. Metal evaporation is performed by heating the target metal to a high enough temperature that it starts to evaporate and deposit onto the substrate of a sample placed above it. Two main methods are used to heat the metal; resistive heating by two large electrodes placed on either side of the metal, and electron beam heating by blasting the top surface of the metal with a high-power electron beam. For all metal evaporations performed in this research the latter method was used. Depositions in this research consisted of either an Aluminum deposition, or a titanium and gold deposition. For top metal electrodes a thin layer of titanium is first deposited as an adhesion layer to the ZnO and then the gold is deposited on top of that; gold directly on ZnO would regularly peel away during the metal liftoff process necessitating the use of a titanium layer. The metal evaporation process is the same for Titanium, Gold, and Aluminum but is conducted at different temperatures as each metal has a different melting and evaporation point. The deposition parameters and rates for each of the three metals is listed below.

Parameter	**Titanium**	**Gold**	**Aluminum**
Min Chamber Pressure (Torr)	$3e^{-6}$	$3e^{-6}$	$3e^{-6}$
Sample Rotation (rpm)	15	15	15
Deposition Time (seconds)	40	80	100
Deposition Rate (A/sec)	5	10	10
Nominal Thickness (A)	200	800	1000

Table 4: Metal evaporation parameters for Titanium, Gold, and Aluminum on a Temscal BJD 1800 metal evaporating system.

3.7.4 Zinc Oxide Sputtering

Zinc Oxide (ZnO) is sputtered using a process like the sputtering of tungsten metal. The primary differences are the target material, deposition gases and power, as well as the sputtering system used. The system used for the deposition of the ZnO was a Denton-22 as opposed to the Kurt Lesker system used for the sputtering of Tungsten. In this research ZnO was deposited on a variety of substrates with both a room temperature (~23°C) substrate and heated (215°C) substrate. Heating the substrate was shown in [30][39] to help improve the c-axis orientation of the ZnO thin films. Following the ZnO deposition, some wafers were annealed in a box furnace at 300°C in another effort to improve the ZnO piezoelectric properties and crystal orientation [40]. The parameters for the ZnO deposition are below, followed by the parameters of the annealing step. Zinc oxide thickness was targeted at one micron. SAW device designs initially targeted a four micron wavelength and the ratio of thickness to wavelength of 0.25 had been shown to yield low insertion losses for both Rayleigh and Sezawa wave modes [23]:

Parameter	**Value**
Chamber Base Pressure (Torr)	$3e^{-6}$
Capman Pressure (mTorr)	4.3
Argon Gas Flow (sccm)	93
Power Supply (watts)	200
Bias Voltage (volts)	318
Burn in time (seconds)	60-1800
Substrate Rotation (rpm)	5
Deposition Time (seconds)	6666
Deposition Rate (Å/second)	1.5
Nominal Thickness (um)	1

Table 5: Zinc Oxide RF sputtering parameters in a Denton-22 Sputtering System. The bias voltage is set by the sputtering system to achieve the target power; this value changes over time. The burn in time was 60 seconds if the previous deposition was ZnO or 30 minutes if the sputtering system had been used for several other materials between depositions.

Parameter	**Value**
Annealing Temperature (deg C)	300
Temperature Ramp (deg C/minute)	40
Annealing Time (minutes)	60

Table 6: Annealing parameters for some ZnO samples using Omegalux LMF-3550 box furnace. Annealing occurred in air; no gases were flowed into the chamber.

3.7.5 Photolithography

The Photolithography process is broken up into 5 sections: Single-layer Photoresist, Multi-layer Photoresists, Direct Writing, Mask Writing, and Mask Aligning. Every process performed at a given step in fabrication requires a protection layer or layers to properly protect areas of the sample that were not interacting with the process; different photoresists offer different protections and purposes depending on the deposition or etch step performed.

3.2.5.1 Single-layer Photoresist (SLPR)

Single-layer photoresists (SLPR) have one major advantage over multi-layer; it's quicker and requires a single application step and a single bake step. In this research the only SLPR used was S1818. This PR was an excellent choice as it spins on very easily, quickly, and provides exceptional protection against a variety of wet and dry etches. S1818 was used for etching ZnO to establish vias to bottom metal and to establish the etch holes to release the resonators. The spin characteristics, bake temperature, and development steps are listed below:

Application Parameter	**Value**
Amount (drops)	8
Spin Speed (rpm)	4000
Ramp Speed (rpm/s)	400
Spin Time (seconds)	60
Edge-bead Removal	Yes
Hard Bake (°C)	110
Hard Bake (seconds)	60
Nominal Thickness (um)	1.8
Develop Parameter	**Value**
Spin Speed (rpm)	500
Developer (brand)	351
Develop Time (seconds)	45
DI Rinse Time (seconds)	30

Table 7: Microposit S1818 G2 Positive Photoresist application parameters and development parameters. 351 developer was used diluted with DI water in a ratio of 1 part 351 to 5 parts DI water.

3.2.5.2 Multi-layer Photoresist (MLPR)

Four photoresists (PRs) were used to establish the best multi-layer stack; SPR 2.1, SPR 0.7, LOL2000 (L2K), and LOR10A. The two SPR series PRs are used to define the features and the L2K and LOR10A are pre-exposed PRs that act as an undercut, liftoff resist. By developing clean features in the top layer PR and then undercutting the bottom layer PR a metal-liftoff process can be completed leaving behind clean features.

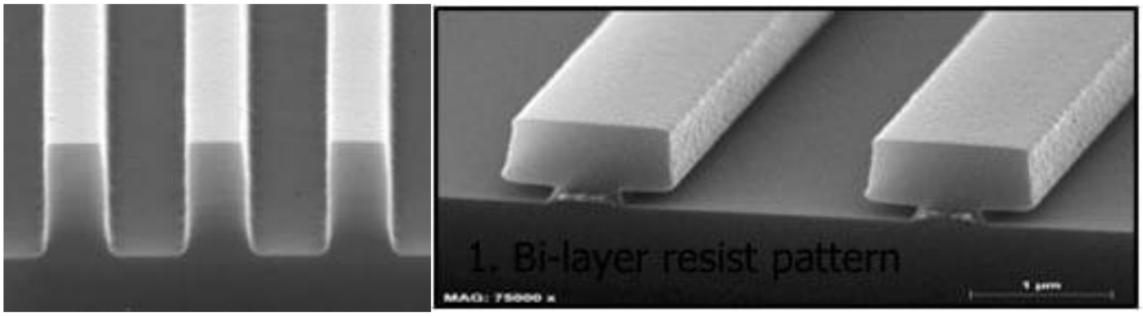

Figure 8: Developed Single layer photoresist (left) vs multi-layer photoresist (right)

The combinations of SPR 0.7/L2K, SPR 0.7/LOR10A, SPR 2.1\L2K, and SPR 2.1/LOR10A were all initially investigated. It was found that the LOR10A tended to spin very poorly onto the 15mm x 15mm samples used in this research. Additionally, the samples with LOR10A tended to develop out of focus regardless of the top PR, development time, or exposure settings. L2K spun on cleanly at 1500, 2000, and 2500 RPM depending on the thickness desired and did not yield any anomalies during developing. SPR 0.7 and SPR 2.1 both yielded the same results for metal liftoff; SPR 0.7 was selected as the top layer resist. The SPR 0.7 and L2K MLPR stack was used for patterning all the metal in this research. The spin characteristics, bake temperatures, and development steps for SPR 0.7 and L2K are listed below:

Application Parameter	**Value (LOL2000)**	**Value (SPR 0.7)**
Amount (droplets)	9	11
Spin Speed (rpm)	1500	4000
Ramp Speed (rpm/s)	1500	400
Spin Time (seconds)	45	30
Edge-bead Removal	Yes	Yes
Hard Bake (°C)	200	110
Hard Bake (seconds)	180	60
Nominal Thickness (nm)	200	700
Developer Parameters for combined PR Stack		
Post Exposure Bake (°C)	110	
Post Exposure Bake (seconds)	90	
Spin Speed (rpm)	500	
Developer (brand)	300MIF	
Develop Time (seconds)	35	
DI Rinse Time (seconds)	30	

Table 8: LOL2000 and SPR 0.7 Positive Photoresist application and develop parameters

3.2.5.3 Direct Writing

After PR is applied to the chips, either a direct write (DW) or a mask aligning (MA) step is completed. DW uses the same machine that would normally write a pattern into a mask and instead writes it directly onto the device substrate. This is used mainly for prototyping. MA is faster whenever more than three or four samples all require the same pattern, but DW benefits from the flexibility of being able to change one feature and immediately rewrite a pattern onto a new device. However, every single photoresist combination, thin film, and substrate can have a large impact on the developed features in a PR after a DW is completed. A Heidelberg DWL 66+ mask writer was used for the direct writes and mask writes required in this research. It could write a 15mm x 15mm pattern in just over three minutes using the “Low-Res” write head and could write the same pattern in about 55 minutes using the “Hi-Res” write head. The Low-Res write head could write features down to approximately 2 microns reliably while the Hi-Res could write features down to 800 nanometers depending on the photoresist used. Initial designs targeted SAW devices with a 4 micron wavelength. Using single electrodes this required a minimum feature size of 1 micron; to realize this, the Hi-Res write head was used. As mentioned previously, the combination of photoresists, ZnO thickness, and substrate all impacted the direct writing performance. The focus parameter for Hi-Res DWs is different for every sample and requires characterization of each sample for ideal results. A four-hour direct write was performed on a sample with the same design patterned 45 times using different focus and laser intensity values. This was done to optimize the parameters for the Hi-Res write head. Over twenty-four unique samples were tested with different substrates, thicknesses, and annealing and sputtering parameters; a four-hour direct write to realize the ideal parameters and then another one-hour direct write to pattern the devices was too time consuming. Therefore, DW was reserved for prototyping new designs. The best parameters for each write head are listed below:

Parameter	**Value (Hi-Res)**	**Value (Low-Res)**
Laser Power (mW)	35	60
Focus offset (%)	18	30
Intensity (%)	65	90
Filter (%)	5	50
Minimum Feature Size (um)	~0.8-1	~1.8-2

Table 9: Direct write parameters for Hi-Res and Low-Res write heads on Heidelberg DWL 66+ mask writer.

3.2.5.4 Mask Writing

Mask writing utilized the Heidelberg DWL 66+ mask writer to create masks for use in a mask aligner. These masks are typically comprised of soda-lime or quartz glass with a thin metal layer and photoresist on top. They are used in a mask aligning tool to transfer the pattern from the mask down to the sample by shining light through the openings in the mask. The masks used in this research were soda-lime glass with chrome metal and AZ1515 photoresist. Masks were made using the Low-Res write head. These masks were then developed, chrome etched, cleaned, plasma ashed, and used in the mask aligner. The parameters used for mask writing are listed below:

Parameter	**Value (Low-Res)**
Laser Power (mW)	60
Focus offset (%)	5
Intensity (%)	90
Filter (%)	50
Minimum Feature Size (um)	~1.8-2

Table 10: Mask writing parameters for Low-Res write head.

3.2.5.5 Mask Aligning

The final step in the photolithography process is mask aligning (MA). This process shines UV light through a mask to transfer a pattern from the mask to the sample. The total dose of UV light, the time that that dose is spread over, and the pattern transfer mode all impact the resolution of the pattern. As mentioned above, the size of the features can also make mask aligning unfeasible. The mask aligner used in this research was a Karl Suss MA-6. The parameters used for this mask aligner are listed below:

Parameter	**Value**
Light Source (wavelength, nanometers)	365
Light Intensity (mW/cm^2)	10.5
Light Power (watts)	300
Operating Mode	Hard Contact
S1818 PR Exposure Time (seconds)	10
SPR 0.7 PR Exposure Time (seconds)	5.5

Table 11: Mask aligning parameters for 15 mm x 15 mm samples using a 4-inch photomask. Exposure times were discovered based on past research and characterized for the specific photoresists used. Adjustments were made to achieve the cleanest possible device features.

3.7.6 Plasma Ashing

Plasma Ashing (PA) is a critical step in the metal liftoff process discussed below. It also is critical to ensure the best performance of a mask. After developing photoresist or after cleaning photoresist off a sample there is regularly a very thin film of photoresist left over. In the case of metal liftoff, a thin layer of photoresist remaining means that the metal will not adhere to the surface and the device will not work. PA uses an oxygen, nitrogen, and/or argon plasma at relatively low power to slowly strip away organic compounds and photoresists. The Anatech Quartz Series plasma asher operating parameters are listed below:

Parameter	**Value**
Chamber Pressure (mTorr)	80
Oxygen Flow (sccm)	550
ICP Power	200
Time (minutes)	2

Table 12: PA parameters for samples. Ashing was conducted prior to any etch step or metal deposition step to ensure developed areas were clean and free of any thin layer of remaining resist.

3.7.7 Wet and Dry Etching of Zinc Oxide and Silicon Dioxide

To create released devices, two main etch steps need to occur. First the ZnO vias are etched. These vias create an opening to the bottom metal and are used to connect the bottom metal to the ground electrode on the top of the device. The second etch step defines the released resonator body and the tethers that anchor the resonator to the substrate. These two processing steps use patterned S1818 PR as an etch-stop to protect the ZnO. A solution of ammonium chloride powder and distilled (DI) water is mixed in a 20% ratio by weight [41]. The ZnO sample is then placed in the solution and lightly agitated for one minute. The sample is transferred to a beaker of DI water and agitated for 15 seconds followed by one minute in a second beaker of DI water. A measurement of the etch rate is then recorded and a final etch time is estimated. The process is repeated until the ZnO is fully etched. The etch would reach a ‘stop’ point before all the ZnO was removed but no more progress could be made. At this point the NH_4Cl would stop etching regardless of how long the sample sat in the solution. This was a result of the bond formed between the ZnO and the interlayer (SiO_2 or Titanium). Buffered Oxide etch (BOE) was used to remove the final, thin layer of ZnO and as a byproduct would remove any remaining SiO_2 interlayer. The etch parameters for ZnO are listed below:

Parameter	**Value**
Solution (% NH_4Cl)	20
Etch Rate (nm/min)	50-200
NH_4Cl Etch (minutes)	5
BOE Etch (minutes)	1
Total Etch Depth (um)	1

Table 13: Zinc Oxide wet etching parameters. The quality of the ZnO film and the underlying film drastically change the etch rates. Depending on the sample etched, the rate fell between 50 and 200 nanometers per minute. This etch rate needs to be established independently for every unique ZnO wafer.

In addition to wet etching, a dry etching recipe was attempted for ZnO based on work in [39] and modified in order to utilized the equipment and gases available and a stable dry etch was developed. This dry etch was slow and not very selective; the PR was etched rapidly as well. The dry etching parameters are listed below:

Parameter	**Value**
Chamber Base Pressure (Torr)	1e-5
Capman Pressure (mTorr)	10
Cl_2 Gas Flow (sccm)	45
Argon Gas Flow (sccm)	15
RIE Power (watts)	200
ICP Power (watts)	500
Etch Time (minutes)*	99.8
Etch Rate Rate (Å/second)	1.67

Table 14: Zinc Oxide Dry etch parameters and measured etch rate. This recipe showed large variance across a single sample and varied etch rates sample to sample indicating this is highly depending on RIE conditions and orientation in the RIE. Etch time listed is theoretical based on a 1 micron thick layer of ZnO.

3.7.8 Metal Liftoff

The metal liftoff process is one way to achieve clean, well defined metal patterns. For any top metal depositions, a metal liftoff process was followed. The sample is prepared by spinning on a multilayer photoresist stack; the sample is then written to via direct writing or a mask alignment. Following that, a post-exposure bake is performed, and the sample is developed using 300MIF developer for 35 seconds. The sample is plasma ashed and then metal is evaporated onto the surface. The liftoff process typically requires three steps, but sometimes requires a fourth to fully remove the metal. First liftoff tape is applied to the top of the sample. It's peeled away from the sample and the metal sitting on top of undeveloped photoresist is peeled away with it, while the metal deposited onto the ZnO stays firmly attached to the surface. Next the sample is spun and sprayed with acetone and isopropyl alcohol to clean off the SPR 0.7 photoresist as well as any remaining metal. Sometimes the metal is adhered too well to the photoresist; in that case the sample is placed in a tray with acetone and put into an ultrasonic water bath for 2-5 minutes. This helps shake the metal loose and allows the acetone to penetrate underneath stuck pieces of metal. Finally, the sample is placed into a holder and lowered into a heated beaker of 1165 developer to remove the LOL2000 photoresist. The parameters used for the removal of the metal and resists is listed below in Table 15. Below that a figure shows a metal liftoff process using LOL2000 as the liftoff resist and a generic imaging resist on top; the process is the same but with SPR 0.7 as the imaging resist.

Parameter	Value
Spin Speed (rpm)	1000
Acetone Spray (seconds)	45
Isopropyl Spray (seconds)	15
1165 Temperature (deg C)	90
1165 Clean (seconds)	120
DI Rinse (cycles)	3

Table 15: Metal Liftoff Parameters to remove SPR 0.7 and LOL2000 photoresists.

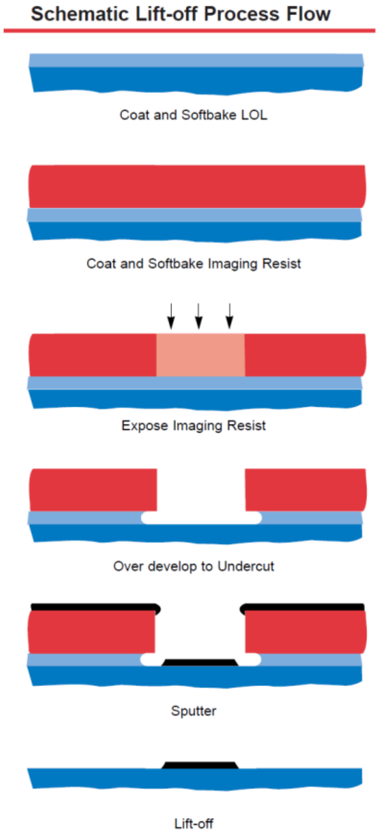

Figure 9: Generic Metal liftoff process.

3.7.9 Tungsten and Titanium Reactive Ion Etching

Reactive ion etching (RIE) was used following the second ZnO wet etch to remove the bottom metal and expose the wafer below. RIE uses a combination of plasma and different gases to launch ions at the surface of the sample to remove a particular layer. By careful selection of the plasma power, and the gases, highly selective etches can be achieved. One sample had a titanium interlayer that needed to be removed. Both released device samples had bottom tungsten metal that needed to be removed and both removal processes utilized RIE. The titanium layer required the use of an Inductively-Coupled-Plasma RIE (ICP-RIE) while the tungsten required a regular RIE. The use of two different machines was due to the gases required for each etch only being available in certain equipment. The parameters for the titanium and tungsten etches are listed below:

Parameter	**W Etch**	**Ti Etch**
Chamber Base Pressure (Torr)	1e-6	1e-5
Capman Pressure (mTorr)	40	5
SF_6 Gas Flow (sccm)	40	--------------
Cl_2 Gas Flow	--------------	40
Ar Gas Flow	--------------	5
RIE Power (watts)	200	75
ICP Power (watts)	--------------	300
Etch Time (seconds)	600	180
Etch Rate Rate (Å/second)	200	2.77

Table 16: Tungsten and Titanium RIE Etch Parameters. Tungsten was etched in an Oxford Instruments PlasmaPro 80 RIE while the Titanium was etched in an Oxford Instruments PlasmaPro 100 Cobra ICP-RIE.

3.7.10 Hydrofluoric Acid Vapor Etching

To fully release the resonators, the thick SiO_2 layer beneath the bottom metal is etched away. This fully separates the bottom of the resonator body from the SiO_2 layer of the SiO_2-on-Silicon wafer and allows the device to resonate. This step is performed in a purpose-built chamber capable of processing Hydrofluoric (HF) acid vapors. It pumps HF vapor, N_2, and methanol vapor into the chamber with the sample; HF etches away oxides while the other gases keep the process stable and carry etchants away from the surface of the sample. Depending on the method used for oxide deposition the etch rate can vary greatly. Both the SiO_2 interlayer on one sample and the ZnO on both samples are affected by the HF. This led to some broken devices on one sample, and complete failure on the other sample. The parameters for the HF vapor etcher are listed below.

Parameter	**Value**
Chamber Running Pressure (mTorr)	133.3
Methanol Vapor Flow (sccm)	400
Nitrogen Gas Flow (sccm)	910
HF Vapor Flow (sccm)	600
Lateral Etch Rate (Å/second)	0.527
Cycle Time (minutes)	15
Cycles (number)	6
One-sided Lateral Etch (um)	28.5

Table 17: HF Vapor Etch Parameters used to etch SiO_2 and undercut devices for release.

3.7.11 Photoresist Removal and Critical Point Drying

Following the SiO_2 removal by HF vapor, the released devices need the protective PR layers removed. The samples were placed into specialized holder placed into a beaker of acetone for five minutes, transferred twice more into fresh beakers of acetone, and then placed into a beaker of methanol. This special holder is designed to work with liquid HF acid and a Tsuomi Critical Point Dryer (CPD). The CPD step is necessary to remove all remaining methanol from the sample. Using pressurized N_2 gas to remove methanol and dry the sample would destroy the devices and small traces of methanol would still be stuck in between the bottom of the released devices and the SiO_2 wafer. The CPD uses liquid CO_2 and a specialized chamber to cool down and then pressurize the sample. Liquid CO_2 is pumped into the chamber to replace any methanol. Then the chamber is heated up: as the pressure and temperature rise a critical point is reached where the CO_2 changes from a liquid to a gas while staying at the same density. This avoids any stiction issues commonly found in alcohol where surface tension between the bottom electrode and the top of the SiO_2 causes liquid to get trapped. Most of the process is automated, the only parameter set by the user is the purge time based on the amount of alcohol added to the chamber when running a CPD. The purge time for ¾ of a chamber of alcohol was 7 minutes.

IV. Testing Methodology

4.1 Testing Methodology Overview

Zinc Oxide samples were characterized before any devices were fabricated using the following two methods: X-Ray Diffractometry (XRD) and Atomic Force Microscopy (AFM). This characterization established a baseline for each sample; this will be used later to compare the working devices to the non-working devices that were testing using electrical measurements of the SAW devices by a network analyzer.

4.2 X-Ray Diffraction

XRD uses an X-Ray emitter and collector pair to identify crystal planes in a sample. The X-Rays are emitted in two parallel, in-phase waves. The emitter rotates clockwise while the collector rotates counterclockwise, each maintaining the same angle relative to the sample. As X-Rays hit the sample they will bounce off different atoms in the sample. At some angles, the X-Rays will reflect off different atoms and be out of phase; these waves will destructively interfere, and a low amount of energy reaches the collector. At other angles, these waves will each hit atoms and reflect back towards the collector in phase, constructively interfering, and a high amount of energy reaches the collector. The angles where the waves constructively interfere identify a particular crystal plane. This basis for the constructive interference is displayed in the figure below:

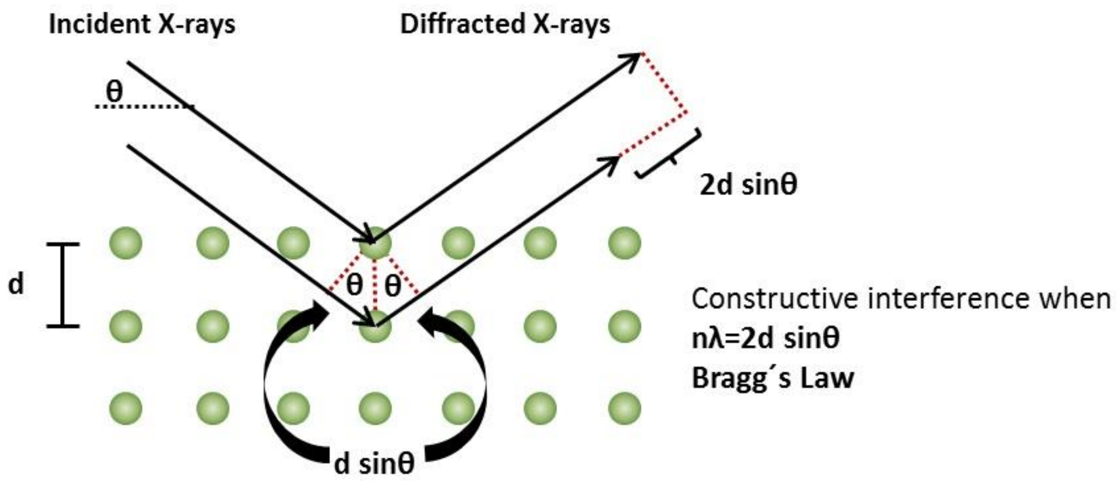

Figure 10: As illustrated above, when incident X-Rays diffract off atoms in the crystal lattice at the correct spacing these diffracted X-Rays will constructively interfere and reach the collector.

The XRD system in this research uses a copper source to generate X-Rays. A high-voltage electron beam is directed at a copper sheet and three characteristic X-Rays are emitted from the copper: $K_{\alpha1}$, $K_{\alpha2}$, and K_{β}. These three X-Rays have slightly different wavelengths and therefore it is possible for a single crystal plane to have up to three associated peaks. A nickel based K_{β} filter was used to remove one of the three peaks, but two remain in some of the collected data. The $K_{\alpha2}$ wavelength is approximately half the intensity of the $K_{\alpha1}$ wavelength and depending on the specific sample, the peak associated with the $K_{\alpha2}$ wavelength may not be seen at all due to its lower intensity.

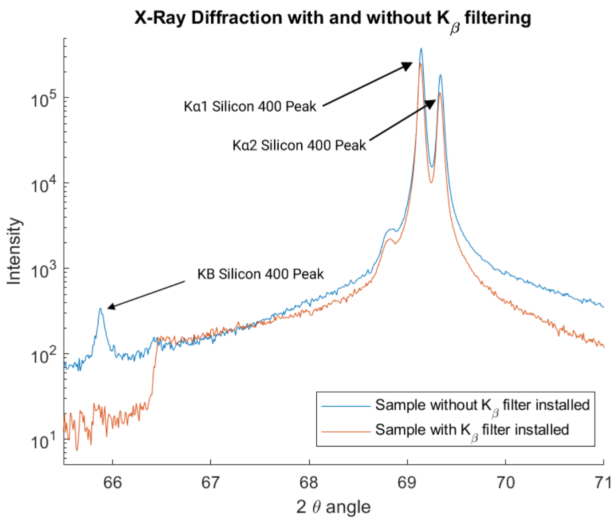

Figure 11: XRD of two samples built on 100 Silicon wafers. The three peaks associated with the Silicon 400 plane are annotated above. With the addition of a Nickel K_β filter one of the peaks is removed helping to clean up data and avoid mischaracterization of peaks.

Each sample was loaded into the XRD and scanned from 20 degrees to 90 degrees of 2θ angle. A Rigaku Smartlab II XRD with a HyPix3000 collector were utilized for all the XRD scans in this research; the scanning parameters are listed below:

Parameter	**Value**
Length Limiting Slit (mm)	10
Solar Slit (mm)	2.5
Scan Type	1-D
Incident Slit (mm)	0.1
Receiving Slit #1 (mm)	20.0
Receiving Slit #2 (mm)	20.1
Start 2θ (degrees)	20
Stop 2θ (degrees)	90
Scan Speed (degrees/minute)	4
Emitter Tube Voltage (kV)	40
Emitter Tube Current (mA)	44

Table 18: XRD Conditions used for scanning ~1 mm thick, 15mm tall samples

4.3 Atomic Force Microscopy

There are many applications of AFM, but this research utilized its ability to measure surface roughness across all tested samples. Surface roughness measurements are calculated by using a small needle on the end of a cantilever to tap the surface of the sample; this tapping allows the system to measure the height of the sample relative to the measurement head. The AFM scans the needle across a fixed distance and then repeats the scan with a slight offset in the y-direction; in this way it creates a 3-dimensional image from repeated 2-dimensional scans. The surface roughness of a sample can give indications of the grain size and shape, as well as the performance of devices on built on that sample. The AFM used in this research was the Bruker Dimension Icon and the scanning parameters are listed below:

Parameter	**Value**
Scan Line Length (nm)	500
Samples/Line	256
Scan Rate (Hz)	0.996
AFM Needle Material	SiN_4
Needle Stiffness (N/m)	0.400
Scan Type	ScanAsyst

Table 19: AFM Scanning Parameters utilized

4.4 Electrical Characterization of Resonators

Electrical characterization of resonators is based on the scattering parameters of the devices. These scattering parameters, or S-Parameters (S11, S22, S12, S21) indicate the input-output relationship between two ports on a device. S11 and S22 show the reflection of power across a frequency range onto ports 1 and 2, respectively. S12 and S21 show the transmittance of power from one port to another across a range of frequencies. The data from these scattering parameters can be used to calculate admittance parameters (Y-Parameters), and the Impedance Parameters (Z-Parameters) of a device.

4.4.1 Parameter Extraction

A common model for to extract equivalent circuit parameters is the Butterworth Van-Dyke (BVD) shown below:

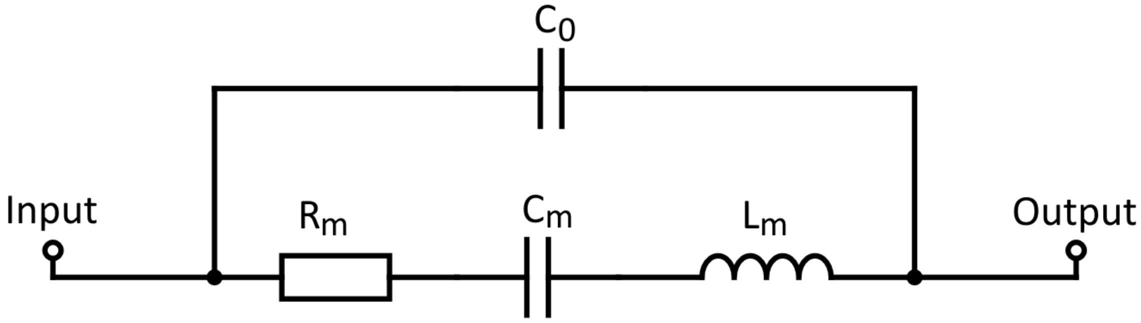

Figure 12: Butterworth Van-Dyke Equivalent Circuit Model. The input and outputs can be considered Port 1 and Port 2 in a 2-Port model. In a 1-Port Model the input would be attached to Port 1 and the output would be grounded.

This model represents a resonator device in terms of its motional resistance, capacitance, and inductance as well as the feed-through, or parasitic capacitance. The equivalent circuit transfer function is listed below:

$$Z_{BVD} = \frac{1}{sC_0}\frac{s^2 L_m C_m + sR_m C_m + 1}{s^2 L_m C_m + sR_m C_m + 1 + \frac{C_m}{C_0}}$$

Equation 20

This transfer function can be decomposed into various relationships that can be solved for based on the measured S-Parameters:

$$w_s = 2 * \pi * f_s \qquad w_p = 2 * \pi * f_p$$

Equation 21

$$w_s = \sqrt{\frac{1}{L_m C_m}}$$

Equation 22

$$w_p = w_s\sqrt{1 + \frac{C_m}{C_0}}$$

Equation 23

$$Q = \frac{1}{w_s R_m C_m} = \frac{w_s L_m}{R_m}$$

Equation 24

Where w_s and w_p are the angular resonant frequencies of the series and parallel resonant response, R_m, C_m, and L_m are the motional resistance, capacitance, and inductance respectively, and C_0 is the parasitic feed-through capacitance. The parameters can be each extracted from the frequency response of a resonator. Each of these parameters will change based on the resonator mode of operation and will need to be calculated individually for each resonant mode. Below is an annotated frequency response curve. One shortcut for measuring Q is to use the series frequency and it’s -3 dB bandwidth using Equation 25 below:

$$Q = \frac{f_0}{\Delta f}$$

Equation 25

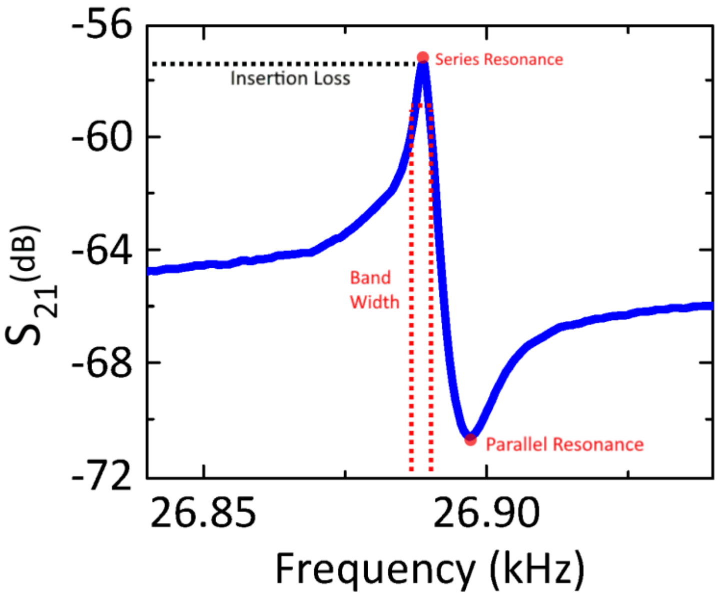

Figure 13: Measured resonance response of SAW device showing the parameters required to complete the BVD parameter extraction.

Series and parallel frequencies can be converted to their angular form using Equation 21 above. Q can be solved for using the measured series resonant frequency and its bandwidth from the figure above. Motional resistance is solved for using the following equation where IL is the annotated insertion loss and R_g is the port impedance of the network analyzer, usually 50Ω:

$$R_m = 2 * R_g \left(10^{\frac{-IL}{20}} - 1\right)$$

Equation 26

Rearranging Equation 20 above, L_m can be solved using known values:

$$L_m = \frac{QR_m}{w_s}$$

Equation 27

Similarly, rearranging Equation 20 in a different way, C_m can be solved:

$$C_m = \frac{1}{w_s R_m Q}$$

Equation 28

And finally, after rearranging Equation 19, C_0 can be solved below:

$$C_0 = \frac{C_m}{\left(\frac{w_p}{w_s}\right)^2 - 1}$$

Equation 29

These calculated values can be used to model the resonator in other software like QUCS Studio or can be used to compare two similar devices to see how their performance differs. Additionally, this parameter extraction can help identify what small fabrication changes can do to the resonator in situations where their measured S_{21} response curves look too similar to make a quantifiable assessment. Below is a measured device as well as its QUCS Studio model overlayed based on the extracted parameters:

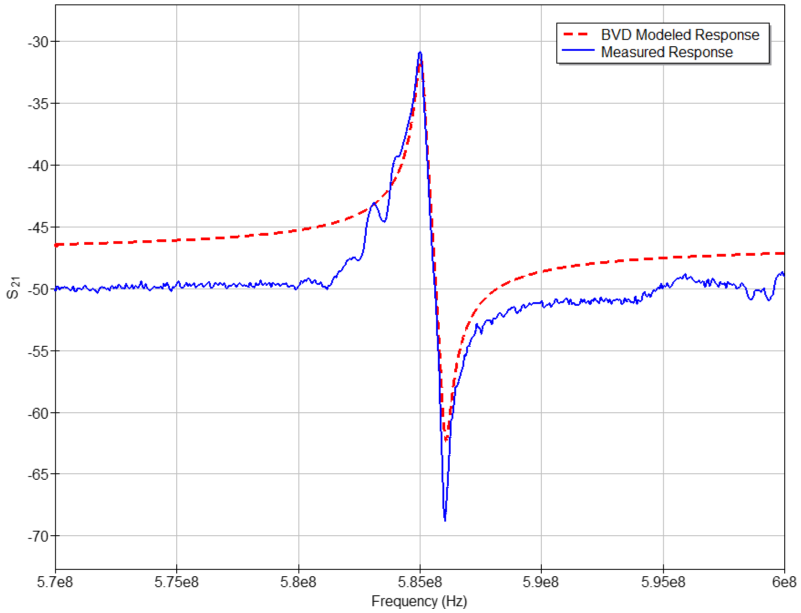

Figure 14: Measured frequency response, S_{21} and the simulated resonator using the extracted parameters calculated with the BVD model equivalence.

4.4.2 Device Testing in Air

The electrical characteristics of SAW devices are measured using a 2-Port Power Network Analyzer (PNA) attached to a set of Ground-Signal-Ground (GSG) Probes. Each set of probes was placed onto the corresponding set of GSG pads on the device and the backside of the sample is placed onto a grounded sample holder. The PNA is set to calculate a fixed number of points of data across a fixed frequency range, both of which are user-set. It is calibrated prior to measurements using a calibration chip to perform a 2-Port Short-Open-Load-Through (SOLT) calibration. This SOLT calibration accounts for any unpredictable resistance on the tips of the GSG probes and any other effects caused by the two coaxial cables connecting the GSG probes to the PNA. Once the calibration is complete the samples are loaded, one at a time, and measurements across the devices are taken. The measured response is displayed on the network analyzer and then saved into an s2p file format containing the S-Parameters.

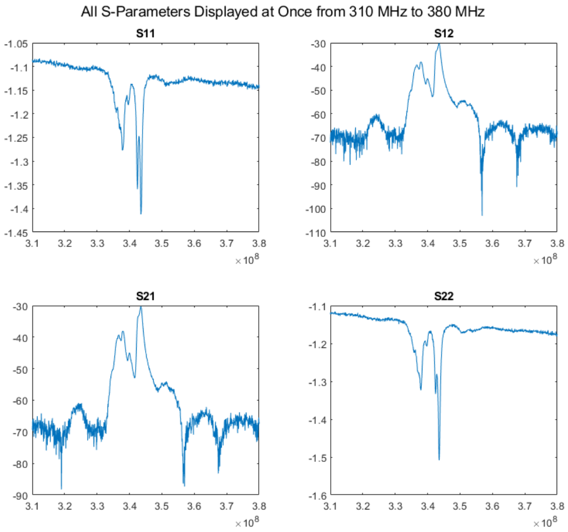

Figure 15: S-Parameters shown together on one chart.

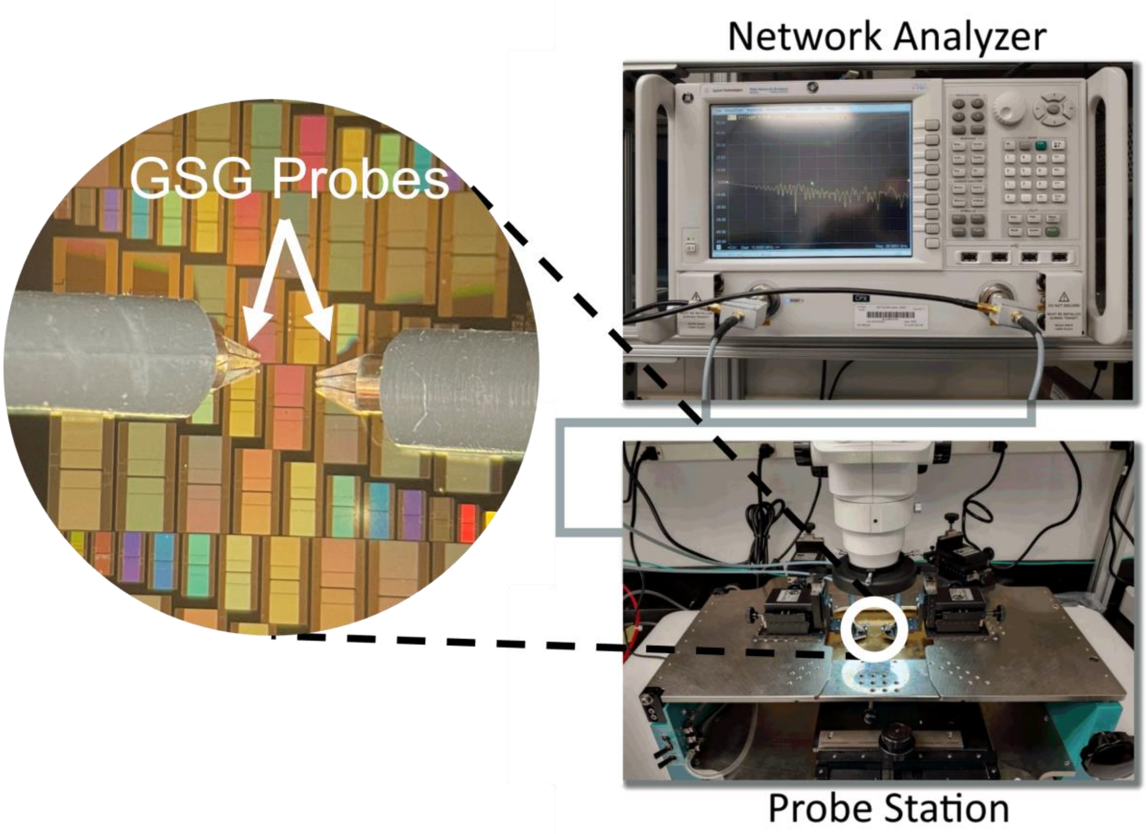

Table 20: Electrical Characterization testing set up. Inset picture shows the GSG Probes above the surface of a sample.

4.4.3 Calculation of Electromechanical Coupling Coefficient

The electromechanical coupling coefficient is a measure of the percentage of electrical energy that is converted to mechanical energy in a device. This coefficient can be calculated in general by the following equation for a 2-port resonator with small coupling coefficients [42]:

$$k^2 = \frac{\pi^2}{4}\frac{f_s}{f_p}\left(1 - \frac{f_s}{f_p}\right)$$

Equation 30

Where f_s and f_p are the series and parallel resonant frequencies. With SAW devices k^2 is also related to the acoustic velocity of the free surface of the unmetallized resonator and the acoustic velocity of the metallized surface by the equation below:

$$k^2 = 2\left(\frac{v_0 - v_m}{v_0}\right)$$

Equation 31

Where v_m is calculated by the f_s of the resonator and the λ value associated with the SAW resonator design. The unmetallized velocity, v_o, can then be solved for by rearranging Equation 31 and using the value calculated for k^2 in Equation 30:

$$v_0 = \frac{-v_m}{\frac{k^2}{2} - 1}$$

Equation 32

By calculating the unmetallized velocity, v_o, Equation 31 can be used to calculate the electromechanical coupling coefficients of the modes of the device more easily, even when the parallel frequency may be hidden in the noise or not displayed at all due to two resonant modes displaying close together.

V. Analysis and Results

5.1 Results Overview

Samples were used to create Zinc Oxide contour mode devices and SAW devices. SAW devices are discussed in more detail in sections below.

- Two ZnO samples, number 23 and 24, were used to create released contour mode LEM and WEM resonators. The fabrication of these devices was attempted twice for each sample type. The released devices did not work and the ZnO thin film on sample 23 had significant residual stress. The devices built on sample 24 had an SiO_2 interlayer between the bottom tungsten metal and the top ZnO thin film. During the HF vapor etching the SiO_2 interlayer was destroyed alongside the sacrificial SiO_2 substrate; this caused the ZnO and top metal layers to peel away from the bottom metal layer rendering the devices ruined.
- SAW devices were fabricated onto three types of substrates with two different deposition temperatures, four combinations of thin films beneath the ZnO, two different annealing parameters, and with varying ZnO deposition thicknesses. A total of 24 unique samples were used for testing different SAW devices. The final SAW fabrication attempt yielded six working devices.

5.2 Zinc Oxide Sample Matrix

Twenty-four unique samples were fabricated. Each sample is listed below with any thin films that were deposited prior to the ZnO deposition as well as the deposition temperature, annealing factor, and ZnO thickness. Samples 1, 2, 3, 4, 14, and 16 all displayed resonance while the remaining eighteen samples did not.

Sample Number	**Substrate**	**Thin Film 1**	**Thin Film 2**	**ZnO Thickness (um)**	**Deposition Temperature °C**	**Annealed Temp °C**	**Resonance**	**Peak Locations (MHz)**
1	Silicon Oxide	X	X	1	22	300	Y	332, 504, 583, 645, 686, 891
2	Silicon Oxide	X	X	2	22	300	Y	332, 501, 576, 672
3	Silicon	X	X	0.7	22	X	Y	484, 726
4	Silicon	X	X	0.7	22	300	Y	723
5	Silicon	X	X	1.52	22	X	N	
6	Silicon	X	X	1.52	22	300	N	
7	Silicon	X	X	1.7	22	X	N	
8	Silicon	X	X	1.7	22	300	N	
9	Silicon Oxide	X	X	1.4	22	X	N	
10	Silicon Oxide	X	X	1.4	22	300	N	
11	Sapphire	X	X	1.34	22	X	N	
12	Sapphire	X	X	1.34	22	300	N	
13	Silicon	X	X	0.91	215	X	N	
14	Silicon	X	X	0.91	215	300	Y	700
15	Silicon Oxide	X	X	0.95	215	X	N	
16	Silicon Oxide	X	X	0.95	215	300	Y	336, 585, 641, 665, 685
17	Sapphire	X	X	0.86	215	X	N	
18	Sapphire	X	X	0.86	215	300	N	
19	Silicon	100nm W	50 nm SiO2	0.85	22	300	N	
20	Silicon	100 nm W	X	0.85	22	300	N	
21	Silicon	50 nm SiO2	X	0.85	22	300	N	
22	Silicon	X	X	0.85	22	300	N	
23	Silicon Oxide	100 nm W	50nm Ti	1	22	300	N	
24	Silicon Oxide	100nm W	50nm SiO2	1	22	300	N	

Table 21: Tested ZnO Samples and their deposition parameters.

Samples 1, 2, 23, and 24 were cut from four different four-inch SiO_2-on-Silicon wafers; Sample 1 had 1 micron of ZnO deposited at room temperature (RT). Sample 2 had 2 microns of ZnO deposited at RT. Sample 23 had 100 nanometers of tungsten metal sputtered at room temperature followed by 50 nanometers of evaporated titanium metal; finally, 1 micron of ZnO was deposited at RT. Sample 24 had 100 nanometers of tungsten metal sputtered at room temperature followed by 50 nanometers of SiO_2 deposited at 300°C using PE-CVD and 1 micron of ZnO deposited at RT. Every wafer was then annealed at 300°C for one hour in air and was diced into 15mm-by-15mm squares.

Samples 19-22 were cut from four different two-inch 100-Silicon wafers and had 850 nanometers of ZnO sputtered onto them at RT. Sample 19 was constructed the same way sample 24 but on a 100-Silicon wafer instead of SiO_2-on-Silicon. Sample 20 was similar to sample 19 but only had the 100 nanometer tungsten layer between the substrate and the ZnO. Sample 21 was like sample 19 but only had the 50nm SiO2 between the substrate and the ZnO. Sample 22 was ZnO deposited directly onto the 100-Silicon wafer. Every wafer was then annealed for one hour at 300°C in air and then diced into 15mm-by-15mm squares.

Samples 3-18 were deposited to establish trends between annealing, deposition temperature, and substrate parameters. Samples 3-8 were deposited at RT onto four-inch 100-Silicon wafers at varying ZnO thicknesses. Each wafer was diced and two samples were set aside from each. One sample was annealed for one hour at 300°C in air and one was kept unannealed. Samples 9-10 were deposited onto a SiO_2-on-Silicon wafer, diced, and then one sample was annealed for one hour at 300°C in air and one was kept unannealed. Samples 11-12 were processed the same way but with c-cut Sapphire wafers. Samples 13-18 used one of each four-inch wafer types and had the ZnO sputtered at a substrate temperature of 215°C. Each wafer was diced and then one sample from each was annealed for one hour at 300°C in air and one sample from each wafer was kept unannealed.

A test structure and five unique devices were fabricated onto each of the twenty-four samples. The device parameters are listed below:

Device	λ	L_a (um)	L_g (um)	L_c (um)	L_{ceff} (um)	L_o (um)	L_p (um)
1	N/A: Through Test Structure						
2	8	180	28	374	N/A	N/A	N/A
3	8	380	28	374	N/A	N/A	N/A
4	8	380	28	366	1166	8	398
5	8	380	28	366	1170	10	398
6	8	380	28	366	1172	11	398

Table 22: Device design parameters. Device 1 is a GSG through test structure to measure the performance of the substrate at transmitting power across top metal. Device 2 is a SAW without reflectors and with a short aperture, L_a. Device 3 is Device 2 with a larger aperture. Devices 4, 5, and 6 have the same aperture as device 3 with reflectors spaced at L_o values of 8, 10, and 11 microns respectively.

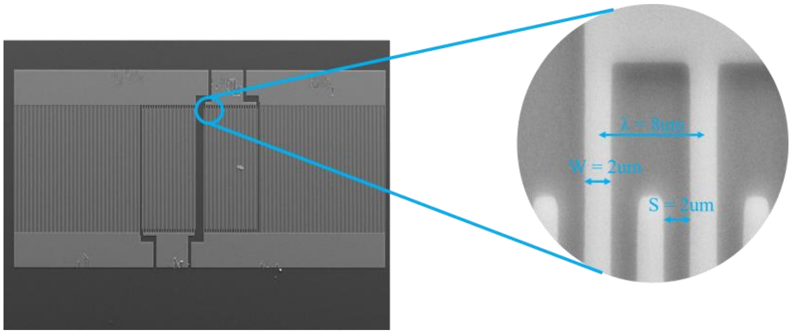

Figure 16: SEM Images of Device 5 on Sample 1

Device 4 is plotted below on the six working samples. The BVD parameters for the Sezawa frequency and the Q and k^2 values are listed below the device plots.

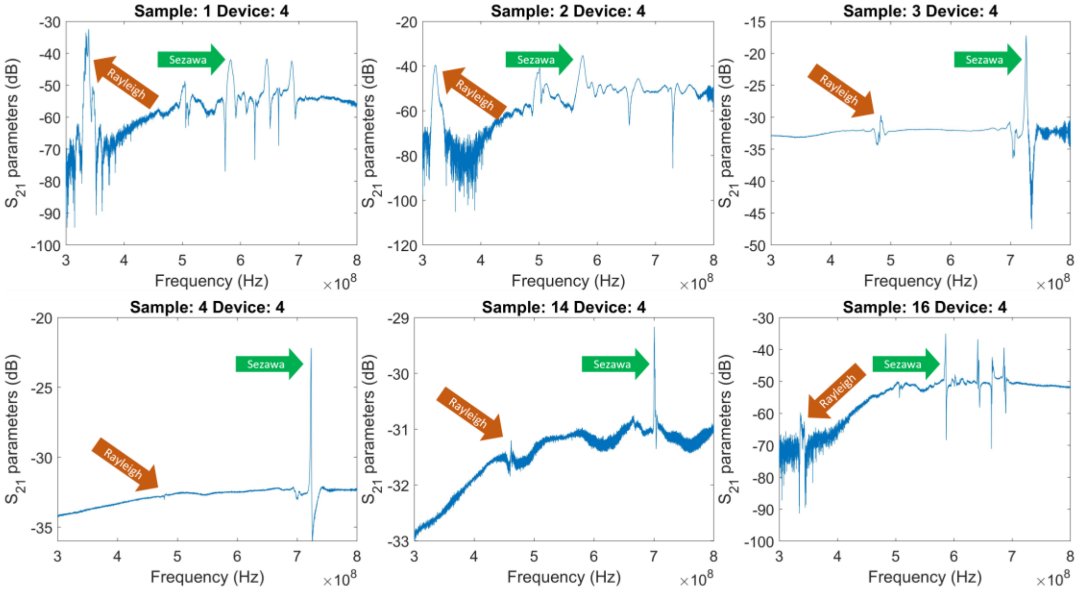

Figure 17: Transmittance Plots of Device 4 (8um reflector spacing)

Sample	f_s	f_p	**3dB BW**	**R_m (Ω)**	**L_m (H)**	**C_m (F)**	**C_0 (F)**	**Q**	**k^2 (%)**
1	582996000	591764000	6447000	12649	0.000312	2.3868 e^{-16}	7.8749 e^{-15}	90.4	3.602
2	574662000	585483000	5672000	5680	0.000159	4.8118 e^{-16}	1.2657 e^{-15}	101.3	4.476
3	726151000	734671000	1445000	638	0.000071	6.8372 e^{-16}	2.8966 e^{-14}	502.5	2.828
4	723104000	725218000	1058000	1188	0.000179	2.7102 e^{-16}	4.6283 e^{-14}	683.4	0.717
14	700841000	703950000		2771					1.084
16	585794000	586727000	466500	5568	0.001899	3.8851 e^{-17}	1.2187 e^{-14}	1255.7	0.392

Table 23: Extracted BVD Parameters for Device 4 on working samples. The Sezawa series and parallel resonant frequencies, the bandwidth (3dB BW) and the Q and k^2 values are charted above. Sample 14's resonant peak was too small to measure a 3dB BW and Q was not able to be calculated; calculation of L_m, C_m, and C_0 is dependent on Q.

The Rayleigh and Sezawa series and parallel resonant wave modes of sample 2 are plotted below:

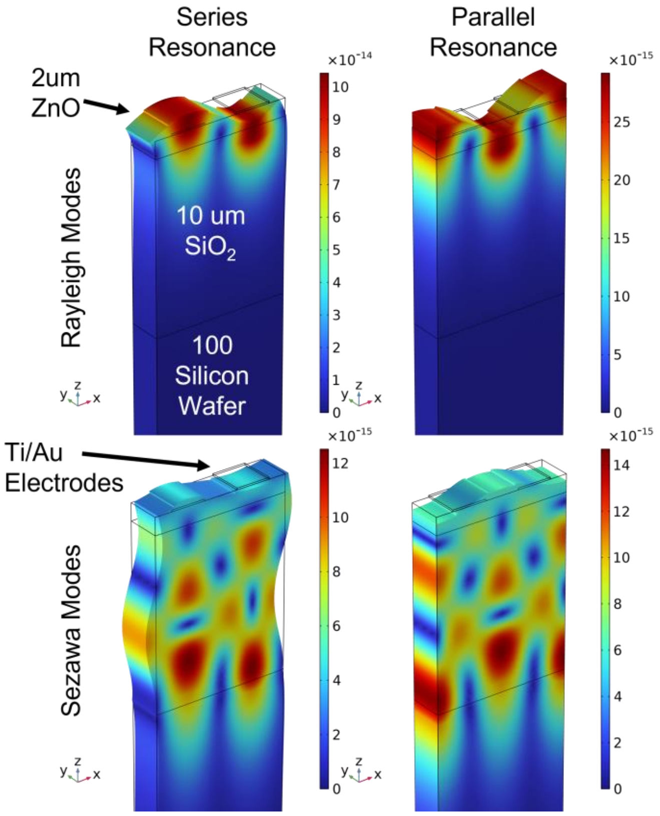

Figure 18: Rayleigh and Sezawa Wave Modes of Sample 2. These graphics are generated using COMSOL Multiphysics Finite Element Analysis Software. Periodic Boundaries are established on the left and right sides as well as the front and back. The top has no

boundary conditions. The bottom of the 100-Silicon Wafer is a fixed constraint. Top electrodes are 2 microns wide with 2 microns spacing in between.

5.3 The Effects of Annealing, Deposition Temperature, and Substrate on ZnO Crystallinity

Each sample was measured by XRD to identify crystal planes associated with the sample. Zinc Oxide has several crystal planes that fall within the scanning region of 20 to 90 degrees 2θ. The (002) plane is present at 34.45° on a 2θ scan with a copper-based X-Ray source. This plane is correlated with a highly c-axis oriented growth structure of the ZnO thin films; c-axis growth is indicative of larger piezoelectric constants and is the preferred orientation for ZnO resonator devices [30].

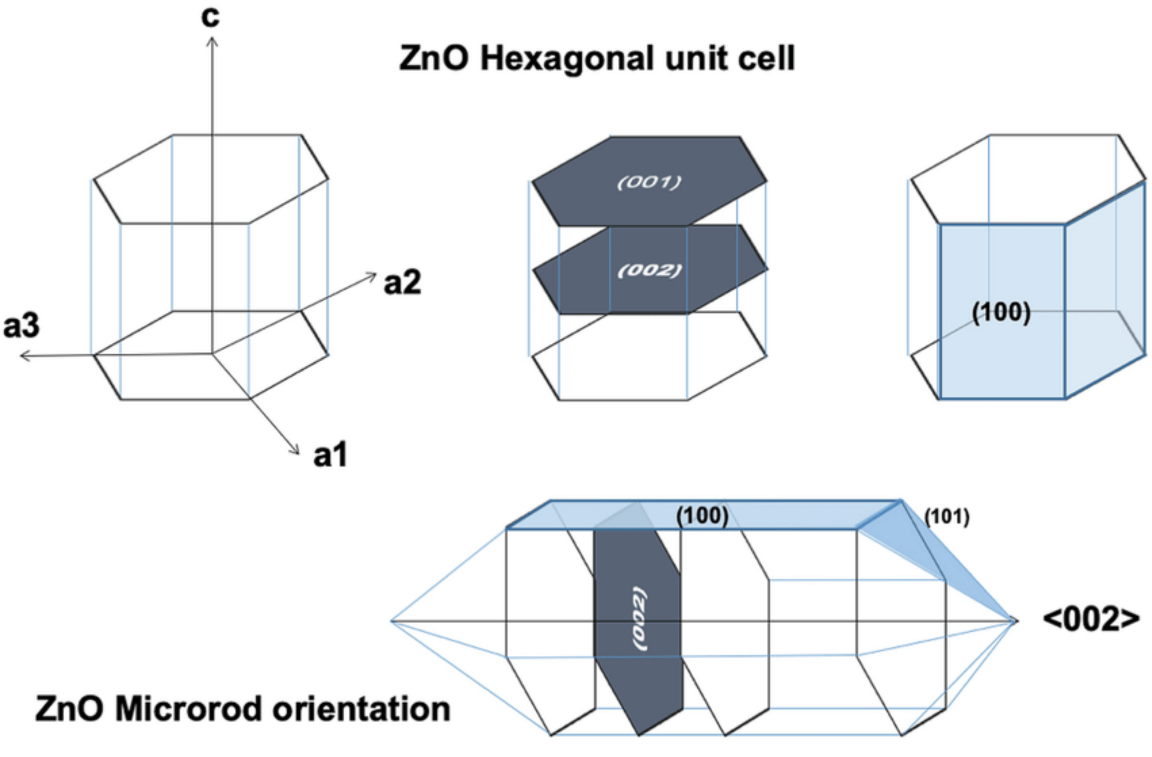

Figure 19: Zinc Oxide crystal plane orientations. Scans from a copper XRD source show the (002) crystal plane at 34.45°. The (002) crystal plane indicated that the ZnO deposited along the c-axis.

The strong presence of other ZnO crystal planes with small FWHM values indicates that the thin film scanned had multiple growth orientations and that SAW devices built on these thin films most likely would not function.

It should be noted that in the presentation of the XRD data below that the intensity associated with each peak is not displayed. Several XRD parameters, as well as the temperature and humidity at the time of scanning, can change the intensity measured at the collector. In addition to the peaks associated with the ZnO, the wafer would exhibit extremely strong peaks based on the exact substrate and its growth structure. Since all the devices were built on similar wafers, XRD data could be normalized between two scans based on the peaks associated with the underlying wafer. However, that still causes variance depending on the day the scan was performed. Full-Width Half-Max (FWHM) measurements can be compared between two samples to give a better indication of the difference in peak width.

Normalized XRD data is presented below for all twenty-four samples between 30° and 40° 2θ. The primary peak of interest, the (002) crystal plane peak, is indicated at 34.45° on the 2θ scan.

Sample Number	100 Peak 31.80° 2θ FWHM	002 Peak 34.45° 2θ FWHM	101 Peak 36.29° 2θ FWHM	102 Peak 47.58° 2θ FWHM	110 Peak 56.66° 2θ IFWHM	004 Peak 72.63° 2θ FWHM
1		**0.2359**				**0.5602**
2		**0.2129**				**0.5120**
3		**0.3220**		**2.0401**		
4		**0.3170**	**0.4602**	**1.0607**		
5	0.2410	0.1530	0.3807	0.7601	0.4502	
6	0.2640	0.1450	0.3506	0.7303	0.4910	
7	0.1420	0.2030	0.2430	0.6210	0.2030	
8	0.1420	0.2240	0.2360	0.5205	0.2570	
9	0.1660	0.1327	0.3020	0.7809	0.3470	
10	0.1730	0.1309	0.2801	1.3509	0.2880	0.1904
11	0.3602	0.3766	0.4090	0.9108		
12	0.2607	0.3414	0.4230	0.7704		
13		0.3150				
14		**0.2980**	**0.3303**		**0.1601**	
15		0.3408				
16		**0.3210**				
17		0.3810	0.2602	0.3810		
18		0.3810	0.2602	0.4720		0.8408
19		0.2813		1.1807		0.6740
20		0.2989				0.7103
21		0.2536		1.0701		0.6030
22		0.3586		2.1802		0.7808
23		0.2341				0.9025
24		0.3810		2.4013	1.3301	0.8801

Table 24: FWHM Values of each tested sample at every ZnO XRD peak within 20 and 90 degrees 2θ. Bolded samples indicate that devices on those samples displayed resonant peaks. Boxes with data indicate the presence of a crystal peak at that 2θ angle. Boxes without data indicate the lack of a crystal peak at that 2θ angle.

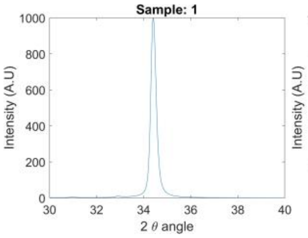
Sample: 1

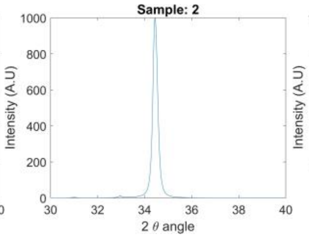
Sample: 2

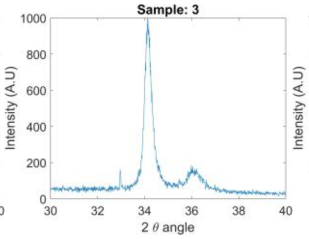
Sample: 3

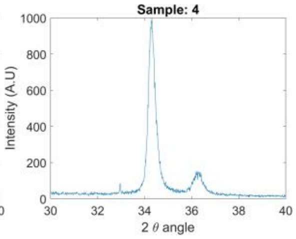
Sample: 4

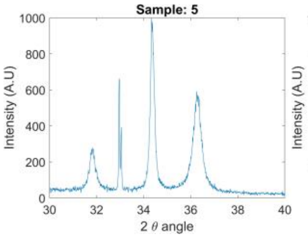
Sample: 5

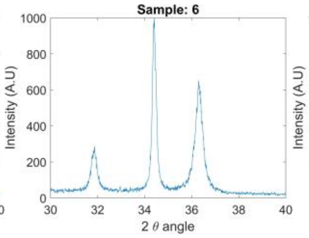
Sample: 6

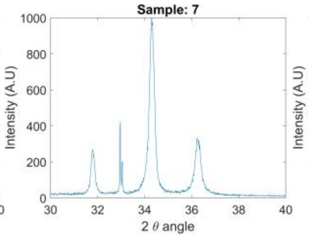
Sample: 7

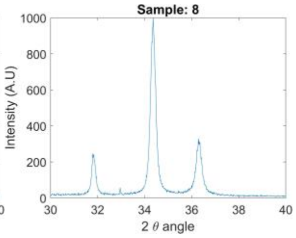
Sample: 8

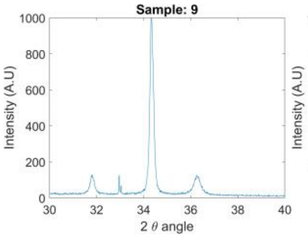
Sample: 9

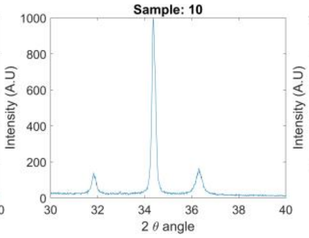
Sample: 10

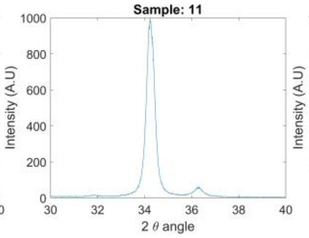
Sample: 11

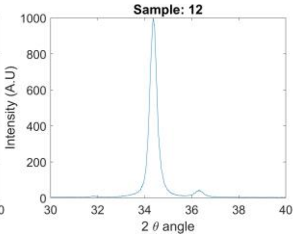
Sample: 12

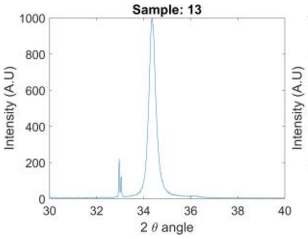
Sample: 13

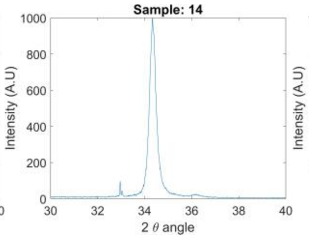
Sample: 14

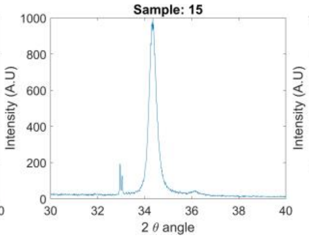
Sample: 15

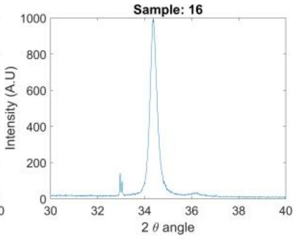
Sample: 16

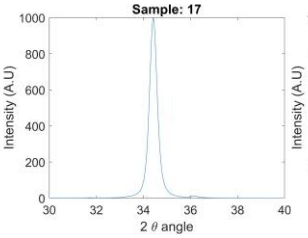
Sample: 17

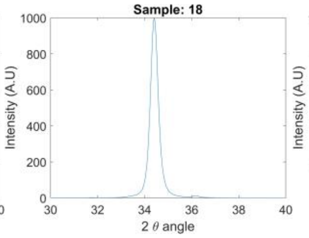
Sample: 18

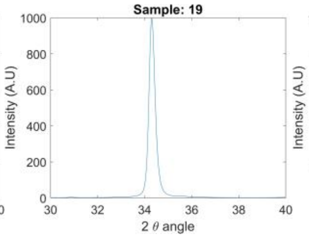
Sample: 19

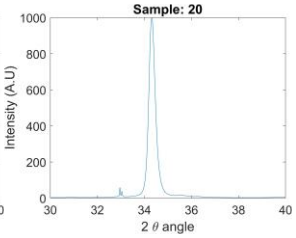
Sample: 20

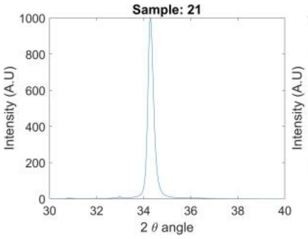
Sample: 21

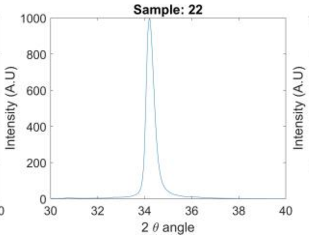
Sample: 22

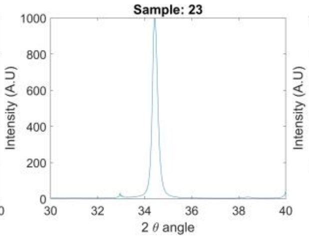
Sample: 23

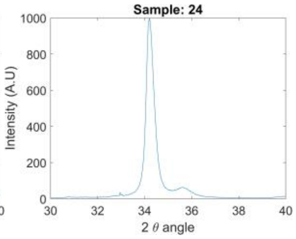
Sample: 24

Figure 20: XRD Plots of samples from 30° to 40° 2θ angle. All plots are normalized to 1000 counts for the (002) crystal peak and plotted on a linear axis.

Samples that had working SAW devices had small FWHM values associated with the (002) ZnO plane and they had either no peaks associated with other crystal planes, or they had very large FWHM values associated with those planes. Several samples in the non-working category had two or more ZnO peaks with small FWHM values associated with their XRD scan. This indicates that the ZnO did not deposit uniformly on those samples; instead ZnO deposited and grew in several different crystal plane orientations. When devices were tested, the electric field applied to those devices was not applied in the appropriate direction relative to the crystal orientation; therefore, strain in the piezoelectric thin film did not occur at all or occurred in several combinations of different x-y-z directions and the energy was dissipated throughout the film rather than across the surface.

Except for samples 7 and 8, every other sample between 3 and 18 showed a decrease in FWHM values on samples that had been annealed at 300°C compared to their unannealed counterpart. This decrease in FWHM values indicates that the crystallite size of the ZnO thin film is larger. This is given by the Scherrer Equation below:

$$FWHM = \frac{K\lambda}{L * \cos\theta}$$

Equation 33

Where K is the shape factor associated with the material, λ is the wavelength of the X-Ray source, L is the crystallite size, and θ is the angle of the measured peak. As FWHM decreases, L must increase since the shape factor associated with ZnO, the XRD wavelength, and the peak angle are not changing. Based on this sample set the following conclusions can be drawn:

- Annealing a Zinc Oxide sample after deposition decreases the FWHM value associated with the preferential (002) ZnO crystal plane. By the Scherrer equation, this decrease in FWHM indicates that the annealed samples have larger crystallites than their unannealed counterparts.
- Depositions that occurred at 215°C had larger FWHM values compared to their RT deposited counterparts. Therefore, they have smaller crystallites formed in the sample during deposition.
- Samples with non-preferential crystal growth were less likely to have functioning devices.

5.4 The Effects of Annealing, Deposition Temperature, and Substrate on Surface Roughness

AFM scans were completed on samples 1 through 22. Root-Mean-Square (RMS) surface roughness (R_q), and the maximum surface roughness (R_{max}) are compared in a table below. The table is sorted by surface roughness with samples with the smallest R_q on top and the largest at the bottom. Highlighted samples are those that had devices that exhibited resonance. All listed samples were scanned with a 500nm-by-500nm area of interest.

Sample Number	***R_q***	**R_{max}**
2	*3.36*	30.5
1	*4.18*	34
22	*5.02*	35.6
4	*5.76*	42.3
3	*6.1*	50.8
19	*6.22*	52.3
21	*6.49*	56.8
12	*7.02*	48
6	*7.33*	51.2
20	*9.1*	66.6
11	*9.13*	72.3
5	*10.5*	89.5
10	*10.9*	83.1
8	*11*	69.2
16	*11*	78.9
9	*11.2*	91
7	*11.4*	69.7
14	*11.7*	72.4
15	*13.3*	81.8
13	*13.6*	99.4
18	*18.3*	120
17	*24.5*	149

Table 25: Samples sorted by R_q, Root Mean Square Surface Roughness. Samples 14 and 16 are outliers as they did have resonance recorded with a larger surface roughness compared to other working devices. Sample 14 had only one resonant peak at the Sezawa frequency mode while the other five samples exhibited Rayleigh and Sezawa frequency modes.

Some samples were scanned with a 5um-by-5um area of interest. Sample 17 exhibited extremely large grains near the surface of the thin film while others, like sample 3, had much smaller, more uniform grains shown in the figure below:

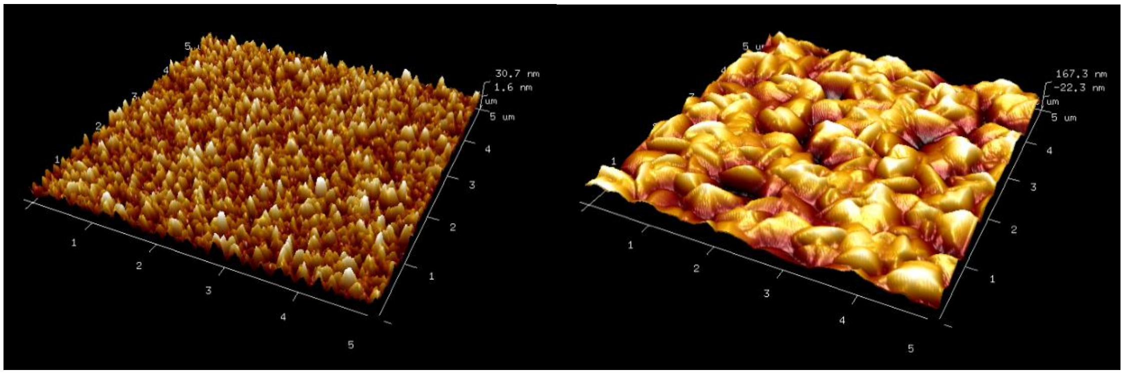

Figure 21: (Left) 5um-by-5um scan of Sample 3, Zinc Oxide deposited onto a 100-Silicon wafer at room temperature, and (Right) 5um-by- 5um scan of Sample 17, Zinc Oxide deposited onto a c-cut Sapphire wafer at 215°C

The R_{max} on sample 17 was greater than 300nm and only 100nm of top metal was deposited onto the samples to pattern the SAW devices. IDTs patterned over regions of large surface roughness may have had metal disconnections resulting in IDTs not operating as designed and leading to device failure.

Larger RMS roughness has a dispersion effect on the SAW waves emitted by the IDTs. This dispersion was shown around 100MHz on Silicon substrates and was extrapolated that the effect would only grow as operating frequency grew [43]. The first frequency of operation of the measured devices in this research is 332 MHz and the dispersion effect could be one of the primary effects causing many SAW devices to show little or no resonance.

There is an increase in piezoelectric constant with increasing grain size [30] and an increase in grain size tends to increase the surface roughness [44]. In other words, SAW devices most likely have a ‘sweet spot’ where the grains are large enough to provide larger piezoelectric constants, but not so large that the resulting RMS roughness allows dispersion effects stop the device from functioning. Large grains and low surface roughness values are possible; the goal is to increase the grain size as much as possible while decreasing the surface roughness. Sample 17 shows incredibly large grains, but also incredibly large surface roughness compared to other samples.

5.5 ZnO SAW Device Results and Discussion

The results from ZnO SAW devices are broken into the following sections:

- The effect of wavelength on Rayleigh and Sezawa operating frequencies, insertion losses, and wave velocities on a single sample
- The effect of sample thickness on Rayleigh and Sezawa operating frequencies, insertion losses, and wave velocities across two samples
- The effect of reflectors and reflector spacings on SAW devices and their operating frequencies, insertion losses, and wave velocities on a single sample
- The effect of substrate selection on the operating frequencies, insertion losses, and wave velocities across tested samples
- The effect of aperture on device performance
- Devices that did not exhibit resonance

5.5.1 The Effect of λ on Device Operation

A set of devices was patterned onto a sample from the same wafer as sample 1. This set of devices was a scaled version of an 8 micron λ device. By scaling the same design, it would maintain the design rules across all devices. Devices at the following λ values, in microns, were observed: 4, 4.8, 5.6, 6.4, 7.2, 8, 9.6, 11.2, 12.8, 14.4, and 16. These represented the initial 8λ design as well as scaled versions from 50% to 200%. There is a strong dependence between the ratio of height of the thin film, h, to wavelength, λ, and the performance of Rayleigh and Sezawa wave modes in relation to the device's IL and k^2. Every combination of layers, ZnO thickness, λ, and electrode material effects performance of Rayleigh and Sezawa modes. The following figures show the insertion losses of the two fundamental modes in relation to the h/λ, as well as the surface wave velocity of ZnO on an SiO_2 wafer as the ratio of h/λ changes:

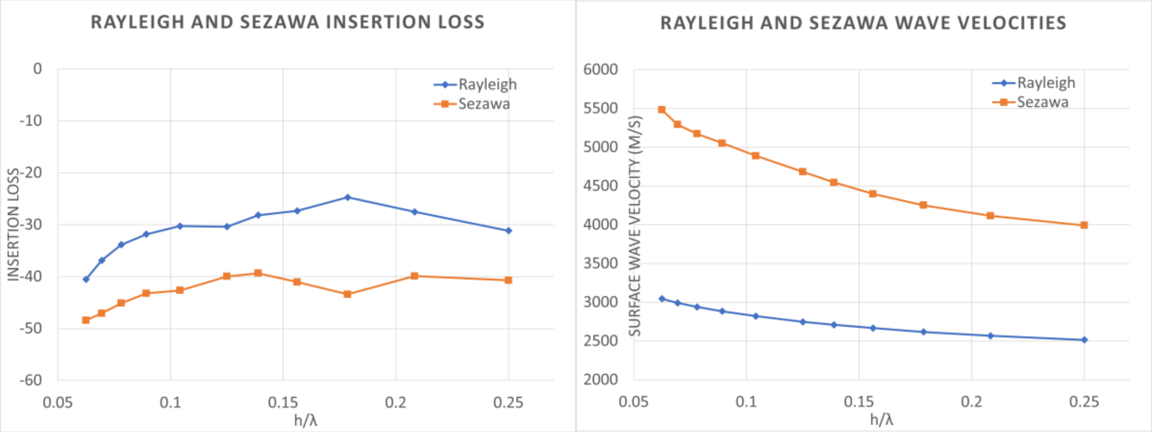

Figure 22: h/λ values and their corresponding Insertion Losses (Left) and the corresponding Wave Velocities (Right). Since h/λ values are inverses of the λ values, the 4um λ devices are displayed on the right side of the data and the 16um λ are shown on the left of each plot. Surface wave velocity calculated by rearranging equation 6 where $v_m = f_0 * \lambda$.

As seen above, the lowest insertion losses for Rayleigh waves were associated with the 5.6 micron λ devices, while the lowest insertion losses for Sezawa waves were associated with the 4.8 micron λ and 7.2 micron λ devices. The ZnO thickness and λ values of the device can be tuned to achieve the lowest IL and therefore the lowest motional resistance in each device. As the h/λ values approaches 0.05, that the insertion loss starts to fall rapidly compared to any other ratio tested. Previous devices fabricated with 32 micron λ on 1 micron of ZnO (0.03125 h/λ) exhibited no resonance. It is assumed that the insertion losses were greater than the noise floor on those devices, but more work is required to test ratios smaller than 0.625 and greater than 0.25.

5.5.2 The Effect of ZnO Thickness on Device Operation

This section will explore the results associated with the samples 1 and 2 and the change in thickness of the ZnO layer. They are characterized by their surface wave velocities at the Rayleigh and Sezawa wave modes as well as the IL of the devices and the Q factor of the tested devices. It should be noted that ZnO devices on SiO2 wafers tend to exhibit significant peak splitting. Additionally, several overlapping modes tend to be observed near key operating frequencies.

Samples 1 and 2 were both characterized as having a small RMS roughness and a small FWHM value at the (002) plane, indicating that the surface was smooth, and the crystallite sizes were large and uniform. Sample 2 had lower RMS roughness and a slightly smaller FWHM value than sample 1. XRD scans performed on the same day showed that sample 2 had roughly four times greater relative intensity over sample 1. Sample 1 ended up having a slightly higher frequency of operation at Rayleigh and Sezawa modes than sample 2. The graph below illustrates the relative performance of the devices. While sample 1 tended to have a smaller IL at the lower frequency Rayleigh mode, sample 2 had a smaller IL at the Sezawa mode:

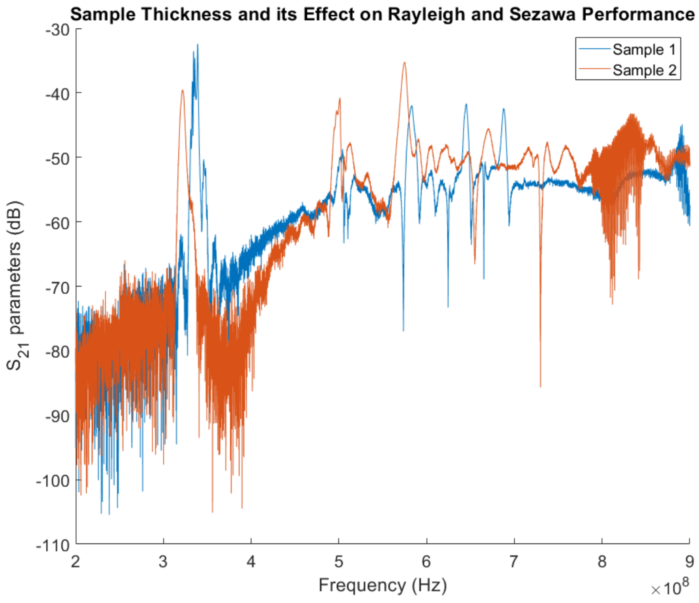

Figure 23: Comparison between sample 1 (1 um thick ZnO) and sample 2 (2 um thick ZnO) and their frequency response on device 4 (8 micron reflector spacing). Sample 2 has lower center frequencies for Rayleigh and Sezawa modes, because the sample has a lower metallized surface acoustic velocity, v_m. These results are in line with the results seen in section 5.5.1. Sample 1 has an h/λ of 0.125 while sample 2 has an h/λ of 0.25. Figure 21 shows that sample 2 has a lower acoustic velocity than sample 1 and therefore a Rayleigh and Sezawa center frequency lower than sample 1

At Rayleigh frequencies, samples 1 and 2 had Q factors of 419 and 72 respectively and k^2 values of 3.43% and 6.58%. At Sezawa frequencies, samples 1 and 2 had Q factors of 90 and 100 and k^2 values of 3.60% and 4.48% respectively. The resonance of each of the devices fundamental modes was wide compared to some of the other samples in this research due to overlapping frequency modes on samples 1 and 2 and their fundamental modes. Sample 1 had a significantly higher Q-Factor for the Rayleigh mode; this was because the coincident mode was not overlapping the Rayleigh mode as much as it was in sample 2; this meant that a much narrower 3dB bandwidth could be measured on sample 1 while the coincident mode overlapping on sample 2 caused the 3dB bandwidth to be much wider.

5.5.3 The Effect of SAW Reflector Spacing on Device Operation

The presence of SAW reflectors is a key factor in improving the insertion loss of a resonator. Placing these reflectors in the correct spot with the correct number of reflector gratings increases the device's performance by lowering the insertion loss. If the reflectors are set up with the wrong spacing, then surface waves reflecting back from the reflectors will destructively interfere with the waves created by the IDTs and the insertion loss of the device will increase. Three reflector spacings were tested on devices fabricated on all the samples. Samples 1, 2, 3, 4, 14 and 16 were the only devices to show resonance and the reflector spacing on those devices will be explored.

In addition to Equation 7, two other calculations were made to establish the resonator spacing L_o:

$$L_0 = N\frac{\lambda_0}{2}$$

Equation 34

$$L_0 = N\frac{\lambda_0}{2} + \frac{\lambda_0}{4}$$

Equation 35

In all these equations, the integer value, N, was set equal to 2. The resulted in three L_o values of 8, 10, and 11 microns of spacing for the reflectors and these are compared below next to devices without any reflectors at all. Below is a chart of the insertion losses associated with the Sezawa mode of each device.

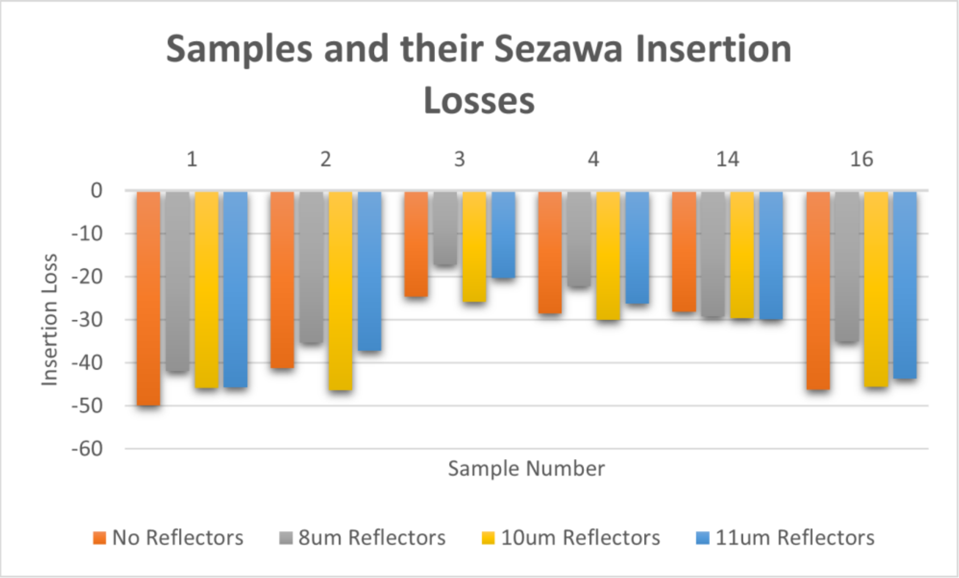

Figure 24: Chart of Insertion Loss associated with each sample's devices with no reflectors, or with reflector spacing at 8, 10, or 11 microns.

Devices on sample 14 are unaffected by the change of reflector spacing and the resonant peak is just 1 or 2 dB larger than the noise floor. This indicates that the resonant mode is incredibly weak and could be due to defects in the sample’s surface or defects in the device. Furthermore, devices fabricated without resonators tend to have worse insertion losses than devices with reflectors; however, devices with reflectors that cause significant destructive interference perform even worse. 10 micron spaced reflectors tested on devices show a larger insertion loss than most of the devices without reflectors. In this sample set, 8 micron spaced reflectors perform better than reflectors spaced at 10 or 11 microns for Sezawa wave modes.

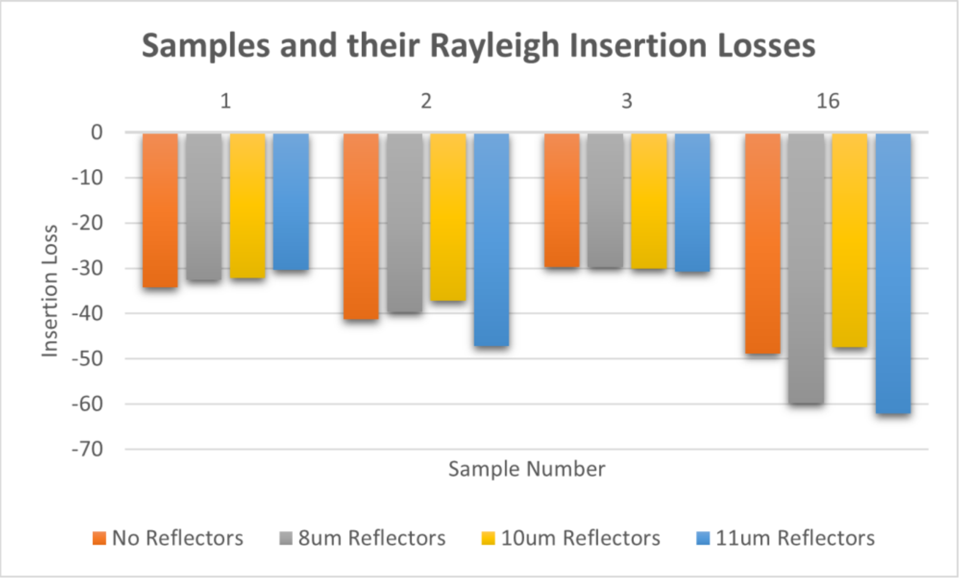

Figure 25: Chart of Insertion Loss associated with the Rayleigh mode devices on each sample with no reflectors, or with reflector spacing at 8, 10, or 11 microns.

Sample 3's devices are not affected by the reflector spacing at the Rayleigh mode while, in general, the Rayleigh mode of operation tends to have a trend opposite the Sezawa mode; reflectors at 10 micron spacing tend to perform better than those at 8 or 11 micron. These two opposing trends are key to fabricating better devices; if the desired operating frequency of a device is associated with the Rayleigh mode, 10 micron spaced reflectors tend to perform better than any of the other tested spacings, while if the desired frequency is at the Sezawa wave mode, the 8 micron spaced reflectors provide smaller insertion losses than the others tested.

5.5.4 The Effect of Substrate Material on Device Operation

Substrate selection makes a difference in the performance and frequencies of SAW resonators. As discussed above, the effective velocity of the surface waves in a thin film is dependent on the properties of the thin film, as well as the properties of the substrate below and the wavelength of the devices fabricated. A substrate with a larger stiffness will cause the surface wave in the thin film to move faster while a smaller stiffness will cause the surface wave to move slower effectively changing the frequency of operation. This effect can be seen in research where ZnO SAWs were built on a Silicon Carbide substrates; the velocity of the ZnO thin films is 1000-3000 m/s greater than the calculated velocity in this research when compared at the same h/λ value [9]. The Rayleigh and Sezawa frequencies of devices built on 100-Silicon are nearly 50% larger than the same devices built on SiO_2-on-Silicon wafers with the same design parameters; this is observed when comparing sample 3 (Silicon) to sample 16 (SiO_2-on-Silicon).

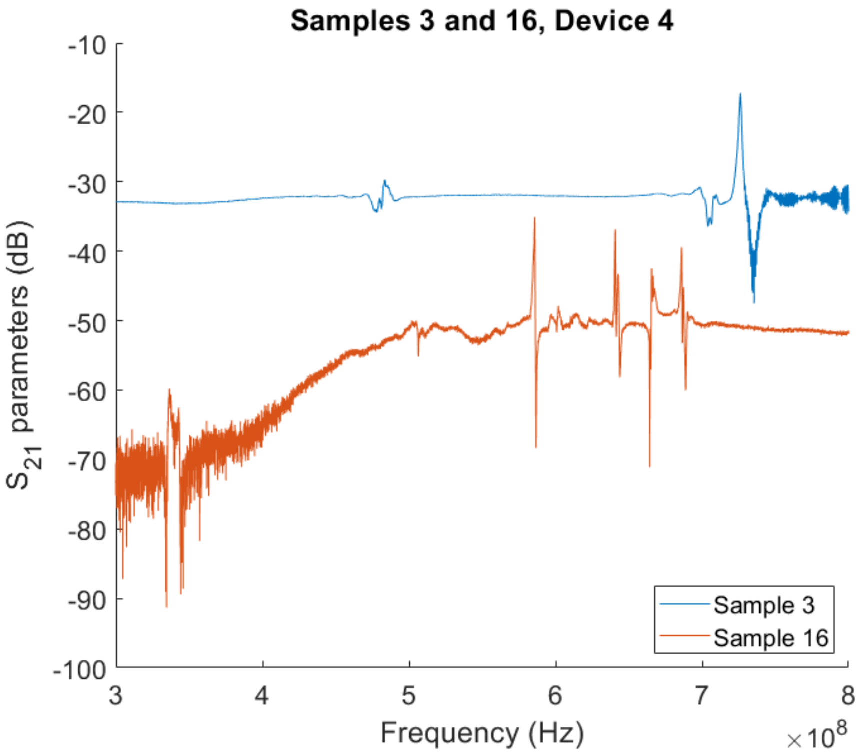

Figure 26: Comparison of Samples 3 and 16. Sample 3, built on Silicon has its Rayleigh frequency of operation at ~484 MHz while sample 16 has its Rayleigh mode at ~330 MHz. The Sezawa modes are located at ~723 MHz for sample 3 and ~585 MHz for sample 16. With the same wavelength this demonstrates a larger v_m for ZnO directly built on a Silicon wafer rather than on a SiO_2-on-Silicon wafer. Additionally, all of the devices

built on silicon have smaller insertion loss indicating that SiO_2 is absorbing and dissipating more of the energy than the Silicon.

Sapphire substrates were also tested in this research but did not yield any working devices. Sapphire substrates and ZnO thin films have a significant lattice mismatch [3] and the results from that mismatch are observed in the XRD data presented above. The lattice mismatch causes significant crystal growth along non-preferential ZnO growth planes even though c-cut sapphire is similar in crystal structure and orientation to (002) ZnO. While (002) ZnO crystal planes were present in the sapphire substrates, the (100), (101), and (102) planes also grew in the bulk of the thin film effectively stopping SAW devices from functioning. It has been shown that ZnO has yielded devices with a high Q-Factor of 30,000 when deposited on sapphire wafers with an aluminum bottom metal layer [21]. The aluminum interlayer in that research helped ZnO deposit at its preferential orientation.

5.5.5 The Effect of Aperture on SAW Devices

Out of the six devices designed, devices 2 and 3 were the only SAW designs without reflectors. Device 2 had an aperture approximately 1/2 the size of devices 3-6. While the comparison between devices 2 and 3 on a given sample do not draw definitive conclusions about the best aperture size, they do show that if the device height is not a major constraint that a larger aperture decreases the insertion loss of a device in every circumstance tested in this research.

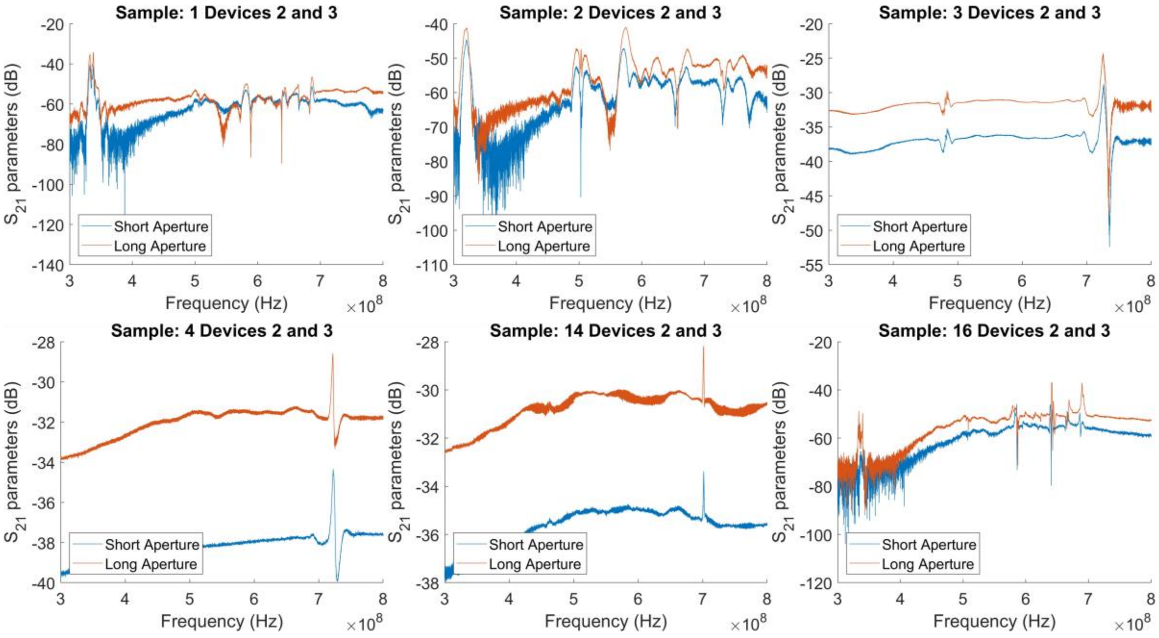

Figure 27: Comparison between a short aperture (device 2) and a long aperture (device 2). The device with the longer aperture decreases the insertion loss by 4 to 8 dB depending on the sample and operating frequency. Since the insertion loss is proportional to the motional resistance of the device, the longer aperture makes these SAW devices have a lower effective resistance and makes them less power hungry as a result.

5.5.6 Samples with Non-Functioning Devices

Some samples in this research did not work. Samples 5-12 had crystal plane growth in several non-preferential directions and failed to yield any working devices. Samples 13 and 15 both had uniform crystal plane growth but large surface roughness and failed to yield working devices. Samples 17 and 18 both had non-uniform crystal plane growth and large surface roughness; devices on these samples did not yield working devices. Samples 19-22 had uniform crystal growth and low surface roughness These four samples sat in a cleanroom environment for 11 months before SAW devices were fabricated onto them. Samples 19 and 21 had yielded working SAW devices previously so it assumed that after sitting for 11 months samples 19-22 had degraded due to an unknown influence. Samples 23 and 24 had uniform crystal growth and low surface roughness but also had tungsten metal and SiO_2 and titanium interlayers. These layers negatively impacted the ZnO in an unknown way and SAW devices on these samples did not function.

VI. Conclusions and Recommendations

6.1 Recommendations for Future Works

There are several aspects of this research that should be improved or modified. With the overall goal of building temperature and vibration resistant ZnO contour mode filters, there needs to be several intermediate steps. At this current point in time, it's unknown whether the lack of resonance of released devices is due to design parameters, material selection, material deposition, or fabrication processes. Each of these variables must be addressed and some of the ways to address them are listed below:

- Purchase commercially deposited c-axis-oriented piezoelectric ZnO. Test device designs and fabrication processes on commercial wafers to validate said designs and processes.
- Purchase new ZnO sputtering target and characterize the deposition on several bottom metal layers by XRD, AFM, and SAW device fabrication.
- Establish faster, more anisotropic ZnO etch recipes to facilitate the fabrication of cleaner sidewalls and enable smaller released designs to be fabricated.

After each of these are addressed and working released devices have been fabricated, new designs should be made to target higher frequencies and then designed to act as filters around those frequencies. For SAW devices there are also several avenues worth traversing to make improvements:

- Create new SAW devices to target and identify the best aperture for a device. Identify the point at which a larger aperture starts hurting device performance rather than improving it.

- Check more reflector spacings to validate the results found in this research and to identify if there exists a better value for the reflector spacing other than what was explored here.
- Test SAW devices using heated and cooled vacuum probe bench to simulate space environment and establish a relationship between temperature and insertion loss and frequency.

  Test SAW devices on a shaker table to establish any potential relationship between vibration and insertion loss and frequency.

6.2 Conclusions on Research

This research has concluded, through experimental measurements, the correlation between device performance and the crystallinity and surface roughness of Zinc Oxide. It was shown that small FWHM values associated with crystal planes other than (002) is one of the biggest indicators of poor or no device performance. Surface Roughness can identify crystal size and deposition uniformity to help identify samples that have a large surface roughness and therefore high likelihood of failure.

Additionally, this research showed that the wavelength of the device relative to the thickness of ZnO on a given sample plays a large role in the performance and wave velocity of the device. This research only looked at h/λ values ranging between 0.0625 and 0.25 but was able to conclude that in this range the best performing Rayleigh modes saw a minimized insertion loss associated with an $h/\lambda = 0.1785$, and Sezawa modes had the best performance at $h/\lambda = 0.1388$. It should be noted that the device performance at h/λ values greater than 0.25 may be significantly higher but was not tested in this research. The relationship between insertion losses and h/λ is non-linear and different for every ZnO thickness and substrate material.

The thickness of ZnO also impacts device performance. At thicknesses of 1 and 2 microns and wavelengths, λ, equal to 8 microns on both samples, it was shown that the increased thickness of the piezoelectric layer reduced the performance of the Rayleigh mode on the device but improved the performance of the Sezawa mode. This should be investigated with more deposited thicknesses to establish a more definitive relationship.

Finally, it was also shown that the insertion loss of a SAW device is heavily dependent on the spacing and presence of the reflector elements on either side of the IDTs. It was shown in this work that the conventional equation for finding the value of the resonator spacing, L_o, is not actually ideal for the Sezawa SAW mode in Zinc Oxide single-IDT devices. The ideal value for the resonator spacing is given by equation 33:

$$L_0 = N\frac{\lambda_0}{2}$$

In Rayleigh SAW Modes the performance of the device increased on some devices with no reflectors present but that result was less conclusive and needs to be investigated further.

VII. Bibliography

[1] L. Gao, Y. Yang, and S. Gong, “A 14.7 GHz Lithium Niobate Acoustic Filter with Fractional Bandwidth of 2.93%,” in *IEEE International Ultrasonics Symposium, IUS*, Sep. 2020, vol. 2020-September, doi: 10.1109/IUS46767.2020.9251795.

[2] O. Khandan, “Titanium MEMS Technology Development for Drug Delivery and Microfluidic Applications,” vol. 3, no. June, p. 2015, 2015, [Online]. Available: http://weekly.cnbnews.com/news/article.html?no=124000.

[3] Y. Q. Fu *et al.*, “Advances in piezoelectric thin films for acoustic biosensors, acoustofluidics and lab-on-chip applications,” *Progress in Materials Science*, vol. 89. Elsevier Ltd, pp. 31–91, Aug. 01, 2017, doi: 10.1016/j.pmatsci.2017.04.006.

[4] H. Kulkarni, K. Zohaib, A. Khusru, and K. Shravan Aiyappa, “Application of piezoelectric technology in automotive systems,” *Mater. Today Proc.*, vol. 5, no. 10, pp. 21299–21304, Jan. 2018, doi: 10.1016/j.matpr.2018.06.532.

[5] S. Rahmati, S. F. Shirazi, and H. Baghayeri, “Piezo-electric head application in a new 3D printing design,” *Rapid Prototyp. J.*, vol. 15, no. 3, pp. 187–191, 2009, doi: 10.1108/13552540910960280.

[6] V. K. Samoei and A. H. Jayatissa, “Zinc Oxide-Based Piezoelectric Pressure Sensor,” vol. 1, no. 419, pp. 1–15, 2021, [Online]. Available: http://arxiv.org/abs/2110.13643.

[7] M. Z. Aslam, V. Jeoti, S. Karuppanan, A. F. Malik, and A. Iqbal, “FEM analysis of sezawa mode SAW sensor for VOC based on CMOS compatible AlN/SiO2/Si multilayer structure,” *Sensors (Switzerland)*, vol. 18, no. 6, 2018, doi: 10.3390/s18061687.

[8] S. Zhang *et al.*, “Surface Acoustic Wave Devices Using Lithium Niobate on Silicon Carbide,” *IEEE Trans. Microw. Theory Tech.*, vol. 68, no. 9, pp. 3653–3666, 2020, doi: 10.1109/TMTT.2020.3006294.

[9] S. Fu *et al.*, “High-frequency surface acoustic wave devices based on ZnO/SiC layered structure,” *IEEE Electron Device Lett.*, vol. 40, no. 1, pp. 103–106, 2019, doi: 10.1109/LED.2018.2881467.

[10] J. A. Bahamonde and I. Kymissis, “A Reconfigurable Surface Acoustic Wave Filter on ZnO/AlGaN/GaN Heterostructure,” *IEEE Trans. Electron Devices*, vol. 67, no. 10, pp. 4507–4514, 2020, doi: 10.1109/TED.2020.3018697.

[11] I. Ahmed, U. Rawat, J.-T. Chen, and D. Weinstein, “Super-High-Frequency Low-Loss Sezawa Mode SAW Devices in a GaN/SiC Platform,” pp. 1–9, 2022, [Online]. Available: http://arxiv.org/abs/2204.12113.

[12] S. Fu *et al.*, “High-frequency surface acoustic wave devices based on ZnO/SiC layered structure,” *IEEE Electron Device Lett.*, vol. 40, no. 1, pp. 103–106, Jan. 2019, doi: 10.1109/LED.2018.2881467.

[13] C. H. Ahn *et al.*, “Encapsulated high frequency (235 kHz), high-Q (100 k) disk resonator gyroscope with electrostatic parametric pump,” *Appl. Phys. Lett.*, vol. 105, no. 24, p. 243504, Dec. 2014, doi: 10.1063/1.4904468.

[14] T. A. Faculty, R. Abdolvand, and I. P. Fulfillment, “Thin-Film Piezoelectric-on-Substrate Resonators and Narrowband Filters Thin-Film Piezoelectric-on-Substrate Resonators and Narrowband Filters,” *Mech. Eng.*, no. April, 2008.

[15] N. Van Toan, M. Toda, Y. Kawai, and T. Ono, “A capacitive silicon resonator with a movable electrode structure for gap width reduction,” *J. Micromechanics*

Microengineering, vol. 24, no. 2, p. 025006, Feb. 2014, doi: 10.1088/0960-1317/24/2/025006.

[16] W. L. Huang, Z. Ren, and C. T. C. Nguyen, “Nickel vibrating micromechanical disk resonator with solid dielectric capacitive-transducer gap,” in *Proceedings of the IEEE International Frequency Control Symposium and Exposition*, 2006, pp. 839–847, doi: 10.1109/FREQ.2006.275499.

[17] Y. Hou, M. Zhang, G. Han, C. Si, Y. Zhao, and J. Ning, “A review: Aluminum nitride MEMS contour-mode resonator,” *J. Semicond.*, vol. 37, no. 10, 2016, doi: 10.1088/1674-4926/37/10/101001.

[18] R. Lu, Y. Yang, and S. Gong, “5 GHz A1 Mode Lateral Overtone Bulk Acoustic Resonators in Thin-Film Lithium Niobate,” in *IEEE International Ultrasonics Symposium, IUS*, Sep. 2020, vol. 2020-Septe, doi: 10.1109/IUS46767.2020.9251334.

[19] A. Daruwalla, H. Wen, C. S. Liu, and F. Ayazi, “Low motional impedance distributed Lamé mode resonators for high frequency timing applications,” *Microsystems Nanoeng.*, vol. 6, no. 1, 2020, doi: 10.1038/s41378-020-0157-z.

[20] Y. C. Chang *et al.*, “Effects of thermal annealing on the characteristics of high frequency fbar devices,” *Coatings*, vol. 11, no. 4, pp. 1–10, 2021, doi: 10.3390/coatings11040397.

[21] M. W. Liu, M. B. Zhu, J. H. Li, and C. H. Wang, “High Q, high frequency, high overtone bulk acoustic resonator with ZnO films,” *J. Zhejiang Univ. Sci. C*, vol. 14, no. 4, pp. 279–282, Apr. 2013, doi: 10.1631/jzus.C12MNT07.

[22] K. Iamsakun, W. Elder, C. D. W. Wilkinson, and R. M. De La Rue, “Surface

acoustic wave devices using electrostrictive transduction," *J. Phys. D. Appl. Phys.*, vol. 8, no. 3, pp. 266–282, 1975, doi: 10.1088/0022-3727/8/3/011.

[23] A. H. Weber, G. Weiss, and S. Hunklinger, "Comparison of Rayleigh and Sezawa wave modes in ZnO-SiO2-Si structures," *Proc. - IEEE Ultrason. Symp.*, pp. 363–366, 1991, doi: 10.1109/ULTSYM.1991.234187.

[24] J. Rodriguez *et al.*, "Direct Detection of Akhiezer Damping in a Silicon MEMS Resonator," *Sci. Rep.*, vol. 9, no. 1, pp. 1–10, Dec. 2019, doi: 10.1038/s41598-019-38847-6.

[25] K. Y. Yasumura *et al.*, "Quality factors in micron- and submicron-thick cantilevers," *J. Microelectromechanical Syst.*, vol. 9, no. 1, pp. 117–125, Mar. 2000, doi: 10.1109/84.825786.

[26] M. L. Schuette *et al.*, "Ionic Metal-Oxide TFTs for Integrated Switching Applications," *IEEE Trans. Electron Devices*, vol. 63, no. 5, pp. 1921–1927, 2016, doi: 10.1109/TED.2016.2544200.

[27] T. Abu Ali *et al.*, "Piezoelectric Properties of Zinc Oxide Thin Films Grown by Plasma-Enhanced Atomic Layer Deposition," *Phys. Status Solidi Appl. Mater. Sci.*, vol. 217, no. 21, pp. 1–6, 2020, doi: 10.1002/pssa.202000319.

[28] S. Humad, R. Abdolvand, G. K. Ho, G. Piazza, and F. Ayazi, "High frequency micromechanical piezo-on-silicon block resonators," *Tech. Dig. - Int. Electron Devices Meet.*, vol. 00, no. c, pp. 957–960, 2003, doi: 10.1109/iedm.2003.1269437.

[29] Y. H. Hsu, J. Lin, and W. C. Tang, "RF sputtered piezoelectric zinc oxide thin film for transducer applications," *J. Mater. Sci. Mater. Electron.*, vol. 19, no. 7, pp.

653–661, 2008, doi: 10.1007/s10854-007-9415-1.

[30] P. Sharma, Z. Guler, and N. Jackson, “Development and characterization of confocal sputtered piezoelectric zinc oxide thin film,” *Vacuum*, vol. 184, no. November 2020, p. 109930, 2021, doi: 10.1016/j.vacuum.2020.109930.

[31] R. Müller *et al.*, “Chemical Vapor Deposition Growth of Zinc Oxide on Sapphire with Methane: Initial Crystal Formation Process,” *Cryst. Growth Des.*, vol. 19, no. 9, pp. 4964–4969, 2019, doi: 10.1021/acs.cgd.9b00181.

[32] R. Serhane *et al.*, “PLD elaboration of piezoelectric ZnO thin film for 540 MHz Al/ZnO/Pt bulk acoustic wave resonator,” *2013 Jt. IEEE Int. Symp. Appl. Ferroelectr. Work. Piezoresponse Force Microsc. ISAF/PFM 2013*, pp. 275–278, 2013, doi: 10.1109/ISAF.2013.6748667.

[33] P. K. Shin, Y. Aya, T. Ikegami, and K. Ebihara, “Application of pulsed laser deposited zinc oxide films to thin film transistor device,” *Thin Solid Films*, vol. 516, no. 12, pp. 3767–3771, Apr. 2008, doi: 10.1016/j.tsf.2007.06.068.

[34] G. Wisz, I. Virt, P. Sagan, P. Potera, and R. Yavorskyi, “Structural, Optical and Electrical Properties of Zinc Oxide Layers Produced by Pulsed Laser Deposition Method,” *Nanoscale Res. Lett.*, vol. 12, no. 1, pp. 0–6, 2017, doi: 10.1186/s11671-017-2033-9.

[35] S. Sinha and S. K. Sarkar, “ZnO as transparent conducting oxide by Atomic Layer Deposition,” *Conf. Rec. IEEE Photovolt. Spec. Conf.*, pp. 1183–1186, 2013, doi: 10.1109/PVSC.2013.6744351.

[36] S. Datta, *Surface acoustic wave devices*. Prentice-Hall, 1986.

[37] D. P. Morgan, “Surface Acoustic Wave Devices,” in *Encyclopedia of RF and*

Microwave Engineering, Hoboken, NJ, USA: John Wiley & Sons, Inc., 2005.

[38] R. Abdolvand, “THIN-FILM PIEZOELECTRIC-ON-Abdolvand, R. (n.d.). THIN-FILM PIEZOELECTRIC-ON-SUBSTRATE RESONATORS AND NARROWBAND FILTERS. Georgia Institute of Technology.SUBSTRATE RESONATORS AND NARROWBAND FILTERS,” Georgia Institute of Technology.

[39] S. Bensmaine and B. Benyoucef, “Effect of the temperature on ZnO thin films deposited by r.f. magnetron,” in *Physics Procedia*, Jan. 2014, vol. 55, pp. 144–149, doi: 10.1016/j.phpro.2014.07.021.

[40] S. Joshi, M. M. Nayak, and K. Rajanna, “Effect of post-deposition annealing on transverse piezoelectric coefficient and vibration sensing performance of ZnO thin films,” *Appl. Surf. Sci.*, vol. 296, pp. 169–176, 2014, doi: 10.1016/j.apsusc.2014.01.067.

[41] J. Sun *et al.*, “Realization of controllable etching for ZnO film by NH 4 Cl aqueous solution and its influence on optical and electrical properties,” *Appl. Surf. Sci.*, vol. 253, no. 11, pp. 5161–5165, Mar. 2007, doi: 10.1016/j.apsusc.2006.11.036.

[42] Y. Zhang, Z. Wang, and J. D. N. Cheeke, “Resonant spectrum method to characterize piezoelectric films in composite resonators,” *IEEE Trans. Ultrason. Ferroelectr. Freq. Control*, vol. 50, no. 3, pp. 321–333, Mar. 2003, doi: 10.1109/TUFFC.2003.1193626.

[43] C. M. Flannery and H. Von Kiedrowski, “Effects of surface roughness on surface acoustic wave propagation in semiconductor materials,” in *Ultrasonics*, May 2002, vol. 40, no. 1–8, pp. 83–87, doi: 10.1016/S0041-624X(02)00095-1.

[44] M. Mirzaee, A. Zendehnam, and S. Miri, “Surface statistical properties of ZnO thin films produced by magnetron sputtering at different rates,” *Sci. Iran.*, vol. 20, no. 3, pp. 1071–1075, 2013, doi: 10.1016/j.scient.2013.05.014.

REPORT DOCUMENTATION PAGE

Form Approved
OMB No. 0704-0188

1. REPORT DATE *(DD-MM-YYYY)*
16-06-2022

2. REPORT TYPE
Master's Thesis

3. DATES COVERED *(From - To)*
September 2020-June 2022

4. TITLE AND SUBTITLE
INFLUENCE OF MATERIALS AND DESIGN PARAMETERS ON SPUTTERED ZINC OXIDE GENERATED SURFACE ACOUSTIC WAVES

5a. CONTRACT NUMBER

5b. GRANT NUMBER

5c. PROGRAM ELEMENT NUMBER

6. AUTHOR(S)
DeWhitt, Samuel B, Capt

5d. PROJECT NUMBER

5e. TASK NUMBER

5f. WORK UNIT NUMBER

7. PERFORMING ORGANIZATION NAME(S) AND ADDRESS(ES)
Air Force Institute of Technology
Graduate School of Engineering and Management (AFIT/ENG)
2950 Hobson Way
Wright-Patterson AFB OH 45433-7765

8. PERFORMING ORGANIZATION REPORT NUMBER
AFIT-ENG-MS-22-J-008

9. SPONSORING/MONITORING AGENCY NAME(S) AND ADDRESS(ES)
Air Force Research Labs Space Vehicles
Dr. Madeleine Naudeau, PI of Advanced GPS Technologies
2000 Wyoming Blvd SE
Albuquerque, NM 87123
madeleine.naudeau@us.af.mil

10. SPONSOR/MONITOR'S ACRONYM(S)
AFRL/RV

11. SPONSOR/MONITOR'S REPORT NUMBER(S)

12. DISTRIBUTION/AVAILABILITY STATEMENT
DISTRUBTION STATEMENT A. APPROVED FOR PUBLIC RELEASE; DISTRIBUTION UNLIMITED.

13. SUPPLEMENTARY NOTES

14. ABSTRACT

This thesis presents research into Zinc Oxide (ZnO) based resonators to include Width Extensional Mode (WEM), Length Extensional Mode (LEM), and Surface Acoustic Wave (SAW) devices. The design and operation of ZnO based SAW devices are investigated further to characterize design parameters and operating modes. Their design, fabrication, and results are discussed in detail. SAW device testing in conjunction with X-Ray Diffractometry (XRD) and Atomic Force Microscopy (AFM) are utilized to characterize ZnO and its deposition parameters on a variety of different substrates and interlayers, with different deposition temperatures and annealing parameters. These substrates include silicon, silicon oxide-on-silicon, and sapphire wafers with interlayers including titanium, tungsten, and silicon oxide. Fabrication methods are discussed to explain all processing steps associated with SAW and released contour mode resonators. The SAW devices in this research test different design parameters to establish better reflector design spacing for higher frequency Sezawa wave modes. The characterization and design of ZnO based SAW devices establishes the potential for prototyping high frequency SAW designs using standard lithography techniques. These devices are desired for space-based operations for use in GPS filters, signal processing, and sensing in satellites and space vehicles.

15. SUBJECT TERMS

16. SECURITY CLASSIFICATION OF:			17. LIMITATION OF ABSTRACT	18. NUMBER OF PAGES	19a. NAME OF RESPONSIBLE PERSON
a. REPORT	b. ABSTRACT	c. THIS PAGE			Dr. Hengky Chandrahalim, AFIT/ENG
					19b. TELEPHONE NUMBER *(Include area code)*
U	U	U	UU	110	(937) 255-6565 x4483 Hengky.Chandrahalim@afit.edu